PONTIFICIA UNIVERSIDAD CATÓLICA DEL PERÚ

ESCUELA DE POSGRADO

AUTOMATIC REGULARIZATION PARAMETER SELECTION FOR THE TOTAL VARIATION MIXED NOISE IMAGE RESTORATION FRAMEWORK

By

Renán A. Rojas

Thesis submitted in partial fulfillment of the requirements for the degree of

Master in Digital Signal and Image Processing

in the Graduate School of the Pontificia Universidad Católica del Perú.

Thesis Supervisor: Paul A. Rodríguez

Examining commitee members:

Jorge R. Chavez

Marco A. Milla

Lima, Perú

November, 2012

Abstract

Image restoration consists in recovering a high quality image estimate based only on observations. This is considered an ill-posed inverse problem, which implies non-unique unstable solutions. Regularization methods allow the introduction of constraints in such problems and assure a stable and unique solution. One of these methods is Total Variation, which has been broadly applied in signal processing tasks such as image denoising, image deconvolution, and image inpainting for multiple noise scenarios. Total Variation features a regularization parameter which defines the solution regularization impact, a crucial step towards its high quality level. Therefore, an optimal selection of the regularization parameter is required. Furthermore, while the classic Total Variation applies its constraint to the entire image, there are multiple scenarios in which this approach is not the most adequate. Defining different regularization levels to different image elements benefits such cases. In this work, an optimal regularization parameter selection framework for Total Variation image restoration is proposed. It covers two noise scenarios: Impulse noise and Impulse over Gaussian Additive noise. A broad study of the state of the art, which covers noise estimation algorithms, risk estimation methods, and Total Variation numerical solutions, is included. In order to approach the optimal parameter estimation problem, several adaptations are proposed in order to create a local-fashioned regularization which requires no a-priori information about the noise level. Quality and performance results, which include the work covered in two recently published articles, show the effectivity of the proposed regularization parameter selection and a great improvement over the global regularization framework, which attains a high quality reconstruction comparable with the state of the art algorithms.

To my parents.

Contents

List of Figures

List of Tables

Chapter 1

Introduction

Total Variation is a well established regularization method widely used in image reconstruction scenarios due to its versatility and its great adjustment to different reconstruction tasks [5, 6, 7]. The constraint this method imposes is a mathematical model coherent with the structure of natural images. Since image restoration's main goal is to obtain an estimate of the original image based on observations, which is an ill-posed inverse problem, such concept limits the set of possible solutions and thus satisfies the uniqueness and stability conditions a well-posed problem requires.

This regularization method features a way of choosing the solution constraint impact based on an element known as regularization parameter. This parameter holds relation with the observation noise level and has a crucial effect in the image estimation quality, which is why it must be selected appropiately [8, 9]. Moreover, extensions of the classic TV functional require multiple regularization parameters [10, 11, 12], which makes of their selection a crucial task. Despite these facts and the wide coverage Total Variation has in the literature, the regularization parameter selection has been mostly left aside. Besides some automatic selection methods [8, 13, 5], a typical approach is to arbitrarily select it.

Since image restoration arises in many practical scenarios, the use of methods such as Total Variation are of major weight in all of them. In fact, every image processing task includes a degradation model [14]. Examples where image restoration is applied go from communication systems to medical imaging. This wide application spectrum implies a wide variety of noise models which deserve a broad study. For instance, Gaussian additive noise usually represents the blurring effect which is typical in data acquisition systems [15, 14, 16]; Impulse noise sources include data transmission or data storage faults; etc. Consequently, several works have extended the Total Variation classic formulation [17] into a more versatile framework. In addition, The research on numerical methods for solving it is still an important matter of study in the literature [10, 18].

The present work focuses on the design of an optimal Total Variation regularization parameter selection framework, which is comparable to the state of the art algorithms. The design concentrates on two noise scenarios: Impulse noise and Impulse over Gaussian Additive noise scenarios. The work includes an insightful view of the regularization parameter impact in the reconstruction quality, along with statistical tools which allow an accurate noise scenario description. This will serve as a mean to study the Total Variation regular-

ization behavior under the noise models of interest in order to design a novel and efficient framework. Also, the present work's preliminary results [1, 4] will serve as backbone for yielding such a scheme.

The rest of the document is organized as follows: Section 2 presents the state of the art methods and concepts required for designing a novel parameter selection framework; Section 3 presents the proposed framework, its stages and their features; Section 4 presents an in-depth evaluation of the proposed algorithm and contrasts it with the state of the art; Finally, Section 5 states the conclusions on the covered topics.

Chapter 2

State of the Art

2.1 Noise Models

Given a noise free image $\mathbf{U} \in \mathbb{R}^{m \times n \times c}$ and its observation $\mathbf{B} \in \mathbb{R}^{m \times n \times c}$, the noise distribution in the observation and its corruption level is crucial information for dealing with an image restoration problem. While there is a wide variety of noise distributions, only two are of interest in the present work: Impulse noise and Impulse over Gaussian Additive noise. For the following subsections, let $b(m,n)$ and $u(m,n)$ denote an element in $\mathbf{B}$ and $\mathbf{U}$, respectively.

2.1.1 Impulse Noise

An Impulse noise corrupted image is represented by the following properties:

$$b(m,n) = I\big(u(m,n)\big) = \begin{cases} i_0 & \text{, with probability}(p_0) \\ i_1 & \text{, with probability}(p_1) \\ \vdots & \\ i_{N-1} & \text{, with probability}(p_{N-1}) \\ u(m,n) & \text{, with probability}(1-\mathbf{p}) \end{cases}$$

where $\mathbf{p} = \sum_{i=0}^{N-1} p_i$. Under this noise scenario, corrupted elements holds no information about its original intensity values.

2.1.2 Additive Noise

An Additive noise corrupted image is represented by the following properties:

$$b(x,y) = A\big(u(m,n)\big) = u(m,n) + \eta(m,n), \tag{2.1}$$

where $\eta(m,n)$, represents a specific noise model. In contrast with Impulse noise, Each element in the image is corrupted, and each holds information about its original value.

2.1.3 Mixed Impulse and Additive Noise

Based on the two previous models, The combination of Impulse and Additive noise is represented in two different ways:

$I\Big(A\big(u(m,n)\big)\Big)$: Impulse over Additive noise scenario.

$A\Big(I\big(u(m,n)\big)\Big)$: Additive over Impulse noise scenario.

It is straightforward to demonstrate that both resulting images are different. A typical and broadly studied Impulse noise scenario is the Salt and Pepper noise model. In it, a corrupted element may only take the minimum intensity value (with probability p_{min}) or the maximum intensity value (with probability p_{max}). For the Additive noise scenario, a typical and broadly studied case is the White Gaussian noise model.

2.2 Total Variation

Let the degradation model for the image restoration problem, i.e. the relationship between an original noise free image u^* and its degraded version or observation b be defined as:

$$b = Ku^* + \eta, \tag{2.2}$$

where η represents an additive noise component, and both original image and observation are vectorized images, i.e. bidimensional signals rearranged as vectors under a certain criteria. The degradation system (K) stability, along with the noise term (η) stochastic nature make this an ill-posed inverse problem [5, 6], which means there may not be a unique stable solution. A useful approach for solving such problems lies in regularization theory [17], which implies giving coherent constraints to the original problem in order to guarantee stablity and uniqueness. This concept is introduced in a strictly mathematical way as a constrained minimization problem:

$$\min_{\mathbf{u}} \|\mathbf{Ku} - \mathbf{b}\|_m^m + \alpha \cdot g(\mathbf{u}), \tag{2.3}$$

The constrained problem is now shown as a cost function in which the optimal solution is represented as the argument $\mathbf{u}$ which minimizes it. This cost function is composed by three elements: i) a fidelity or data fitting term $\big(\|\mathbf{Ku} - \mathbf{b}\|_m^m\big)$, ii) a regularization or penalization term $\big(g(\mathbf{u})\big)$, and iii) a regularization parameter (α). The regularization term introduces a constraint or prior information the solution must satisfy, so it works as a condition the solution must attain and thus stabilizes the initial problem. The fidelity term responds to the fact that, even though the observation contains perturbations, it also contains valuable information about its original structure and features. This term allows the solution to keep such structural information. Finally, the regularization parameter establishes a weighting or balance between both mentioned terms, in order to define the level of similarity to the observation and the level of penalization the solution may hold. The functional represents an unconstrained cost function based on the original problem, as seen on Lagrangian theory [19].

The regularization term introduces constraints based on mathematical models, which must be coherent with the original signal nature. Such constraints include Tikhonov regularization, Wavelet regularization, and Total Variation regularization [5].

In [17], the use of Total Variation as a penalization criterion is introduced into regularization theory. The Total Variation of a signal u is defined as:

$$TV(u) = \int_{\sigma_x} |\nabla u(x)| dx, \tag{2.4}$$

where the function gradient is represented as

$$|\nabla u(x)| = \frac{\delta u}{\delta x}, \tag{2.5}$$

for a one dimensional function u, or

$$TV = \int\int_{\sigma_{x,y}} |\nabla u(x,y)| dxdy, \tag{2.6}$$

where the gradient magnitude is represented as

$$|\nabla u(x,y)| = \sqrt{\frac{\delta u}{\delta x}^2 + \frac{\delta u}{\delta y}^2}, \tag{2.7}$$

for a two dimensional function u. Based on its continuous definition, the Total Variation disrete version is expressed as:

$$TV(u) = \sum_{\Omega} |\nabla u| = \|\nabla u\|_1, \tag{2.8}$$

where the gradient magnitude is represented as

$$|\nabla u(x)| = D_x u, \tag{2.9}$$

for a one dimensional function u, or

$$|\nabla u(x,y)| = \sqrt{D_x u(x,y)^2 + D_y u(x,y)^2}, \tag{2.10}$$

for a two dimensional function u. D_x and D_y represent horizontal and vertical discrete derivative operators, respectively.

Total Variation has a remarkable property which explains its versatility as part of the regularization term. The following Lemma [20] shows the main feature of such a constraint:

$$\min_u TV(u) \quad s.t. \quad u(0) = a, u(1) = b, \quad u : R \to R, \tag{2.11}$$

has as minimizer a monotonic in $[a, b]$, not necessarily continuous function $\hat{u}$ satisfying $\hat{u}(0) = a$, $\hat{u}(1) = b$ and $TV(\hat{u}) = |b - a|$. Figure 2.1 shows the possible solution subset for this problem and how oscillatory functions such as u_5 may not be part of it. As the Figure shows, function u_5 is not monotonic in its defined domain, and since it has a highly

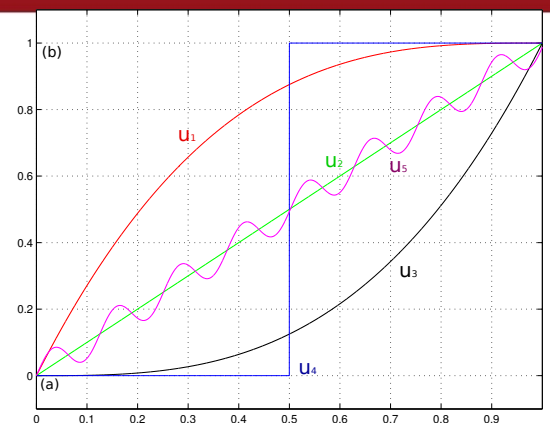

Figure 2.1: Total Variation on one dimensional functions.

oscilatory nature, $TV(u_5) > |b-a|$. Thus, it is not an element in the solution subset.

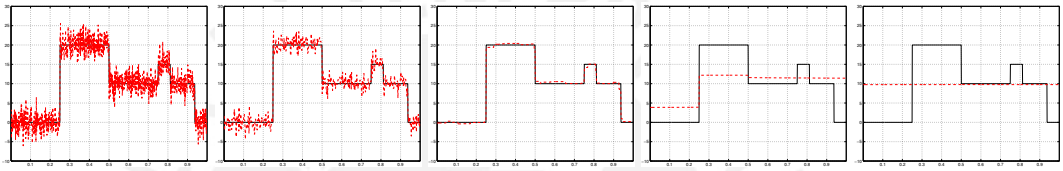

(a) $\alpha = 10^{-4}$ (b) $\alpha = 10^{-3}$ (c) $\alpha = 10^{-2}$ (d) $\alpha = 10^{-1}$ (e) $\alpha = 1$

Figure 2.2: Regularization parameter impact for one dimensional functions. Red: Estimated signal. Black: Original signal.

(a) $\alpha = 10^{-4}$ (b) $\alpha = 10^{-3}$ (c) $\alpha = 10^{-2}$ (d) $\alpha = 10^{-1}$ (e) $\alpha = 1$

Figure 2.3: Regularization parameter impact for two dimensional normalized functions ($\in [0, 1]$).

Equation (2.11) shows how the solution for the minimization problem does not favor a specific kind of function, whether smooth or edge-structured. Moreover, it rejects oscillatory solutions while preserving edges. As a consequence, the Total Variation term is a favorable element for the image restoration problem which preserves features and adapts to a specific desired fitting level.

Following this concept, the Total Variation regularization cost function is described as:

$$\min_{\mathbf{u}} \|\mathbf{Ku} - \mathbf{b}\|_m^m + \lambda TV(u). \tag{2.12}$$

In this formulation, increasing λ results in an increase in the constraint impact and a decrease in the reconstruction - observation similarity, i.e. an increase in the regularization weight and a decrease in the similarity weight.

The Total Variation regularization approach may be summarized in a phrase: "Find a solution which approximates to the observation, but which has a minimum Total Variation". It is shown that the cost function solution is unique and its existence can be proven under certain assumptions [17]. Solving this functional is a complex task since it is not differentiable [5, 6, 21]. Moreover, the regularization approach can also be seen as a scale selection based on λ, by which a certain level of detail preservation is defined. Figures 2.2 and 2.3 show the impact of the regularization parameter in the restoration of one dimensional and two dimensional signals, respectively.

Finally, given an observation $\mathbf{B} \in \mathbb{R}^{m \times n \times c}$, the Total Variation constraint is introduced by characterizing the solution $\mathbf{U}^* \in \mathbb{R}^{m \times n \times c}$ as:

$$\mathbf{u}^* = \arg\min_{\mathbf{u}} \frac{1}{m} \left\| \mathbf{K}\mathbf{u} - \mathbf{b} \right\|_m^m + \frac{\lambda}{n} \left\| \nabla \mathbf{u} \right\|_n^n, \tag{2.13}$$

where $\mathbf{u}^*, \mathbf{b}$ are vectorized versions of the estimated image and the observation, respectively. $\nabla \mathbf{u}$ represents the solution gradient magnitude, which can be modelled as its isotropic version ($|\nabla \mathbf{u}| = \sqrt{\sum_{n \in c} (D_x \mathbf{u}_n)^2 + (D_y \mathbf{u}_n)^2}$) or its anisotropic version ($|\nabla \mathbf{u}| = |D_x \mathbf{u}| + |D_y \mathbf{u}|$). For $c = \{1, 2, 3\}$ we have that $\mathbf{u} = [(\mathbf{u}_1)^T (\mathbf{u}_2)^T (\mathbf{u}_3)^T]^T$ is a 1D vector that represents a 2D color image. Both cost function terms consist on vector norms defined by $(m, n \in \mathbb{R}^+)$.

The classic Total Variation formulation proposed on [17] focused on the Additive noise model scenario and consisted on an ℓ^2 data fidelity term and an ℓ^1 regularization term:

$$\mathbf{u}^* = \arg\min_{\mathbf{u}} \frac{1}{2} \left\| \mathbf{K}\mathbf{u} - \mathbf{b} \right\|_2^2 + \lambda \left\| \nabla \mathbf{u} \right\|_1. \tag{2.14}$$

Although typically used on previous approaches, the fidelity term norm was kept since, for the statistics field, it was considered the best smooth edge-preserving cost function for such a noise model. On the other hand, several data fitting functions and their impact as fidelity terms have been studied in [22, 19]. It is shown that non-smooth data fidelity terms reach high quality minimizers for corrupted images characterized by containing non corrupted elements and outliers, which is the case of the Impulse noise model. The ℓ^1 data fidelity term proofs to be more accurate for this scenario than the ℓ^2 term [14]. This approach is formulated as:

$$\mathbf{u}^* = \arg\min_{\mathbf{u}} \left\| \mathbf{K}\mathbf{u} - \mathbf{b} \right\|_1 + \lambda \left\| \nabla \mathbf{u} \right\|_1. \tag{2.15}$$

2.3 Risk Estimation

A common risk metric for defining the level of likeness between two signals based on the ℓ^2 norm is the Mean Squared Error (MSE) [5]:

$$\text{MSE}(\mathbf{x}, \mathbf{y}) = \frac{1}{n} \sum_{i=0}^{n-1} \big(x(i) - y(i)\big)^2, \tag{2.16}$$

where $x, y \in \mathbb{R}^n$. This tool is able to characterize the reconstructed image quality level, but only if the original image is available.

An alternative way for measuring the reconstruction quality level is by using an unbiased risk estimator, which does not require the original signal. Although the use of such metrics were originally confined to the White Gaussian noise case, its study and applications has been widely covered in the literature [8, 9].

2.3.1 Unbiased Predictive Risk Estimator

The Unbiased Predictive Risk Estimator (UPRE), also known as C_L method [5], for the Total Variation framework was proposed in [9]. As its original formulation, which was intended for the Tikhonov Regularization method, the UPRE estimates the MSE of u_λ for $\mathbf{b} = \mathbf{K}\mathbf{u} + \eta$, where $\eta \sim N(0, \sigma^2)$. UPRE$_{TK}$ is formulated as

$$\text{UPRE}_{\text{TK}}(\lambda) = \frac{1}{n}||r_\lambda||_2^2 + \frac{2\sigma^2}{n} tr(A_{\text{TK},\lambda}) - \sigma^2, \tag{2.17}$$

$$\mathbf{r}_\lambda = \mathbf{K}\mathbf{u}_\lambda - \mathbf{b} \tag{2.18}$$

$$A_{\text{TK},\lambda} = \mathbf{K}(\mathbf{K}^T\mathbf{K} + \lambda\mathbf{I})^{-1}\mathbf{K}^T. \tag{2.19}$$

where $\mathbf{u}_\lambda$ represents $\mathbf{u}^*$ for a specific λ. Given this risk estimation, it is possible to find the optimal λ value by searching in the λ space. Extending this concept to the Total Variation framework, UPRE$_{TV}$ is denoted as

$$\text{UPRE}_{\text{TV}}(\lambda) = \frac{1}{n}||\mathbf{r}_\lambda||^2 + \frac{2\sigma^2}{n} tr\big(A_{\text{TV},\lambda}\big) - \sigma^2, \tag{2.20}$$

$$A_{\text{TV},\lambda} = \mathbf{K}(\mathbf{K}^T\mathbf{K} + \lambda L(\mathbf{u}_\lambda))^{-1}\mathbf{K}^T, \tag{2.21}$$

$$L(\mathbf{u}_\lambda) = D_x^T \text{diag}\big(\Psi'(\mathbf{u}_\lambda)\big) D_x + D_y^T \text{diag}\big(\Psi'(\mathbf{u}_\lambda)\big) D_y. \tag{2.22}$$

Since there is no linear operator than can describe the Total Variation solution, function A, which depends on $\mathbf{u}_\lambda$ is introduced. The Total Variation regularization term is approximated by

$$||\mathbf{u}||_{\text{TV}} = ||\psi\big((D_x\mathbf{u})^2 + (D_y\mathbf{u})^2\big)||_1, \tag{2.23}$$

$$\psi(\mathbf{u}) = \sqrt{\mathbf{u} + \beta^2}, \tag{2.24}$$

where $\psi(\mathbf{u})$ is a smooth approximation of the absolute value function which allows differentiation at the origin.

UPRE$_{\text{TV}}$ inserts in the original formulation a parameter which depends on x_λ. This implies that a solution x_λ must be computed first, which increases the method's computational cost. Besides, [9] points out the high computational cost for computing Trace$\big(A_{\text{TV},\lambda}\big)$, given the fact that in regular cases the images of interest are of a considerable size, and so A dimensions dramatically increase. This problem is approached by means of the Hutchinson Trace estimator [5]. While a Monte-Carlo framework based on Gauss quadrature to obtain the trace is presented in the literature, we propose a rather simple approach to find the trace

estimation.

Let the Hutchinson trace estimator be defined as:

$$E(u^T f(A)u) \simeq \text{Trace}(f(A)) \tag{2.25}$$

where u is a vector which entries are values 1 or -1 with 0.5 probabilities each. It has been proven that

$$\frac{1}{N}\sum_{n=0}^{N-1}(u_n^T f(A)u_n) \simeq \text{Trace}(f(A)), \tag{2.26}$$

where $N << M$, $A \in M \times M$. So, it is required to solve

$$u_n^T f(A)u_n = u_n^T \mathbf{K}\left(\mathbf{K}^T\mathbf{K} + \lambda L(\mathbf{u}_\lambda)\right)^{-1}\mathbf{K}^T u_n. \tag{2.27}$$

The proposed approach, in contrast with the original approach in [9], is to solve:

$$K^T(K(r)) + \lambda L(\mathbf{u}_\lambda)r = v \tag{2.28}$$

for r, where $v = K^T(u)$. Furthermore, $L(\mathbf{u}_\lambda)r$ may be represented as

$$D_x^T(\Psi'(\mathbf{u}_\lambda) \bullet Dx(r)) + D_y^T(\Psi'(\mathbf{u}_\lambda) \bullet Dy(r)). \tag{2.29}$$

So, this procedure requires a linear solver to estimate Trace(A).

2.3.2 Q Metric

In [23], The Q metric, a pseudo-local signal to noise ratio, is presented. Its formulation is based on the estimation of the gradient covariance matrix and its singular value decomposition. Based on this, the gradient's dominant orientations and its energy characterizes each image patch in order to define its structure properties. This no-reference metric quantifies the image "coherence measure", allowing the analysis of the noise level in non-homoskedastic scenarios without depending on its model. It requires no prior knowledge about the noise variance.

The Q Metric is defined as:

$$Q = s_1 R, \tag{2.30}$$

$$R = \frac{s_1 - s_2}{s_1 + s_2}, \tag{2.31}$$

$$G = USV^T = U\begin{pmatrix} s_1 & 0 \\ 0 & s_2 \end{pmatrix}\begin{pmatrix} v_1 \\ v_2 \end{pmatrix}, \tag{2.32}$$

$$G = \begin{pmatrix} p_x(1) & p_y(1) \\ \vdots & \vdots \\ p_x(n) & p_y(n) \end{pmatrix}, \tag{2.33}$$

where (s_1, s_2) are the singular values of the local region gradient matrix G, and n represents

the elements on a neighborhood W_n. Under this formulation, s_1 represents the gradient's dominant orientation, while s_2 represents its perpendicular direction ($s_1 \geq s_2 \geq 0$).

The metric requires consistent gradient components in the analyzed patches in order to obtain a good noise estimate. Thus, it is not capable of defining the noise level in homogeneous regions. The basic idea behind this metric is the level of "structure features" covered by each patch. So, for high noise levels, it is demonstrated that this metric is innacurate, mainly because the loss of structure.

2.4 Impulse Noise Set Estimation

For Mixed noise scenarios, the original Total Variation approach may suffer from bad responses since it affects the entire image in the same way. Different approaches have been proposed in order to attack this issue, most of them based on the addition of terms to the cost function in order to fit the noise distributions. Figure 2.4 shows results from [1], a recent work based on the proposed method's preliminary stages, and displays the reconstruction benefits of local vs. global restoration. A special case for this scenario is the Impulse over Gaussian Additive noise. Since the distortion introduced by it remains unchanged by the others, the corrupted pixel set may be easily identified.

In [2], this approach is used on the Salt and Pepper noise scenario by applying a local noise detector for finding the corrupted pixel set, and then treating them by applying a median filter. Then, the same concept is applied for a variational scheme by penalizing the corrupted pixel set only. Following this idea, a study on different Impulse noise detectors is presented.

2.4.1 Ranked Over Adaptive Median Filter

The Salt and Pepper noise detector based on an adaptive median filter applied in [2, Algorithm 1] is described. The noise pixel set of the observed image $\mathbf{b}$ with L channels is defined by:

$$\mathcal{N} : \{n \in C, l \in \Omega : \hat{b}_n^{w_n^l}(l) \neq b_n(l) \wedge b_n(l) \in \{\mathrm{v}_{min},\ \mathrm{v}_{max}\}\}, \tag{2.34}$$

where $\hat{b}_n^{w_n^l}(l)$ is the output of the Ranked Over Based Adaptive Median Filter (RAMF) [24]. This filter analyzes $\mathcal{K}$, a $(2 \cdot w_n^l + 1) \times (2 \cdot w_n^l + 1)$ neighborhood centered at l in order to define whether this pixel is noise-corrupted or not. The neighborhood size is increased if the median of the neighborhood is equal to its minimum or maximun value, and the procedure is repeated until it reaches a maximum size w_{max}. Then, l is defined as a noise-corrupted pixel if it is equal to the maximum or minimum value in the neighborhood, in which case is replaced by the neighborhood median. In [2], manually selected values for w_{max} are applied depending on the noise level.

The proposed algorithm defines the set W, which is zero if the element l is noise-free and w_n^l if it is noisy. This gives information about the local noise level for each noise-corrupted pixel. Moreover, the global noise level $\mathbf{p}$ can be estimated as $\tilde{p} = \frac{1}{N}\sum \mathrm{I}_{[W \neq 0]}$, where N is the number of pixels and I is the indicator function.

(a) Original image (b) 90% noisy image

(c) 90% Global regularization reconstruction (d) 90% Local regularization reconstruction

Figure 2.4: Global versus local regularization approaches, as shown on the present work preliminary results [1].

2.4.2 Progressive Switching Median Filter

In [25], a progressive switching median filter (PSM) is proposed for treating images corrupted by Salt and Pepper noise. Its general framework is composed by an outlier detector for defining the noise pixel set, and a median filter for restoring it. Regarding the noise set estimation, the algorithm base its criteria in the median absolute difference (MAD). For this purpose, an iterative scheme is used, where an element is defined as corrupted if its observation is over a threshold. f_i defines if the i-th element belongs to the noise set:

$$f_i^{(n)} = \begin{cases} f_i^{(n-1)} & ,|u_i^{(n-1)} - m_i^{(n-1)}| < T_d \\ 1 & , \text{else} \end{cases}$$

where m_i is the median value of a neighborhood centered at the i-th element. Initially, all the elements are assumed to be uncorrupted ($\mathbf{f}^{(0)} = \mathbf{0}$). Based on the output of each

iteration, the element intensities of the observation are modified in order to cope with the iterative scheme:

$$u_i^{(n)} = \begin{cases} m_i^{(n-1)} & ,f_i^{(n)} \neq f_i^{(n-1)} \\ u_i^{(n-1)} & ,f_i^{(n)} = f_i^{(n-1)} \end{cases}$$

After a number of iterations, the noise pixel set is defined by $f_i^{(n)}$. T_d is chosen based on the noise level (p), which is based on an estimation with the same criteria:

$$p = \frac{\sum_{i=0}^{n-1} \hat{p}_i}{n-1} \tag{2.35}$$

$$\hat{p}_i = \begin{cases} 0 & ,|u_i - m_i| < T_0 \\ 1 & ,\text{else} \end{cases}$$

2.4.3 Impulse Weighting Function

In [26], an extension of the Bilateral filter introduced in [27] is proposed. A new weighting component is proposed based on the ROAD (Ranked-over Absolute Difference) statistic, which, in contrast with the Two-Stage methods, gives a continuous function of how much an element is "Impulse-like" or not. This new component, which will be called Impulse Weighting Function (IWF) is defined as:

$$w_I(x) = e^{-\frac{ROAD(x)^2}{2\sigma_j^2}} \tag{2.36}$$

where σ_j is a tunable parameter which defines the weighting penalization degree. By applying a threshold to the function response, it is possible to classify the image elements into a two-stage scheme.

2.4.4 Directional Weighted Median Filter

A novel median filter intended for detecting Impulse noise was proposed in [28]. This directional weighted median filter (DWMF) features a weighting which depends on the intensity differences between local elements on four main directions. This design bases in the fact that a noise free image is characterized by locally smooth areas separated by edges.

The difference on each direction shows if the smooth local region assumption is satisfied based on how big the variability on its main direction is. Following this, the intensity difference on each direction is defined as:

$$d_{i,j}^{(k)} = \sum_{(s,t)\in S_k} w_{s,t}|y_{i+s,j+t} - y_{i,j}|, \tag{2.37}$$

where $w_{s,t}$ describes a weighting function which gives more emphasis to the elements closer to the central pixel. Based on this measurement, the minimum is used as an index for the level of region variability:

$$r_{i,j} = min\{d_{i,j}^{(k)} : 1 \leq k \leq 4\}. \tag{2.38}$$

An Impulse noise element should be characterized by big differences in all four directions due to its outlier nature, while edge elements and elements in flat regions should at least have one small difference. Thus, large $r_{i,j}$ values correspond to outliers. Figure 2.5 shows the four main directions.

-2,2	-1,2	0,2	1,2	2,2
-2,1	-1,1	0,1	1,1	2,1
-2,0	-1,0	0,0	1,0	2,0
-2,-1	-1,-1	0,-1	1,-1	2,-1
-2,-2	-1,-2	0,-2	1,-2	2,-2

$$S_1 = \{(-2,-2);(-1,-1);(0,0);(1,1);(2,2)\}$$
$$S_2 = \{(0,-2);(0,-1);(0,0);(0,1);(0,2)\}$$
$$S_3 = \{(2,-2);(1,-1);(0,0);(-1,1);(-2,2)\}$$
$$S_4 = \{(-2,0);(-1,0);(0,0);(1,0);(2,0)\}$$

Figure 2.5: Directional Weighted Median Filter: Main gradient directions.

2.4.5 Fuzzy Impulse Noise Detection

In [29], the Fuzzy Impulse noise Detection and Reduction Method (FIDRM) is introduced. Its noise estimation stage is a fuzzy-ruled system established based in the GOA filter [30]. Fuzzy gradient values for an element are defined by applying a membership degree function to the element finite difference based gradients, which are taken between the element and its eight neighbors.

$$\Delta_{c,d}I(a,b) = I(a+c,b+d) - I(a,b); \quad (a,b,c,d) \in \{-1,0,1\} \tag{2.39}$$

Each pixel features eight basic gradients, each with two related gradients associated, which are its two finite difference gradient neighbors in the same direction. Figure 2.6 shows the eight basic gradient and their related gradients, as well as the main directions. Fuzzy rules for identifying Impulse noise pixels are based on membership functions for the gradients magnitude and sign. Algorithm 1 shows the applied fuzzy rules.

-2,2	-1,2	0,2	1,2	2,2
-2,1	-1,1	0,1	1,1	2,1
-2,0	-1,0	0,0	1,0	2,0
-2,-1	-1,-1	0,-1	1,-1	2,-1
-2,-2	-1,-2	0,-2	1,-2	2,-2

dir.	basic	related		
N	$\Delta_{(-1,-1)}I(0,0)$	$\Delta_{(-1,-1)}I(1,-1)$	;	$\Delta_{(-1,-1)}I(-1,1)$
NW	$\Delta_{(-1,0)}I(0,0)$	$\Delta_{(-1,0)}I(0,-1)$	;	$\Delta_{(-1,0)}I(0,1)$
NE	$\Delta_{(-1,1)}I(0,0)$	$\Delta_{(-1,1)}I(-1,-1)$	;	$\Delta_{(-1,1)}I(1,1)$
W	$\Delta_{(0,-1)}I(0,0)$	$\Delta_{(0,-1)}I(-1,0)$	;	$\Delta_{(0,-1)}I(1,0)$
E	$\Delta_{(0,1)}I(0,0)$	$\Delta_{(0,1)}I(0,-1)$	;	$\Delta_{(0,1)}I(0,1)$
SW	$\Delta_{(1,-1)}I(0,0)$	$\Delta_{(1,-1)}I(-1,-1)$	;	$\Delta_{(1,-1)}I(1,1)$
S	$\Delta_{(1,0)}I(0,0)$	$\Delta_{(1,0)}I(-1,0)$	;	$\Delta_{(1,0)}I(1,0)$
SE	$\Delta_{(1,1)}I(0,0)$	$\Delta_{(1,1)}I(0,0)$	;	$\Delta_{(1,1)}I(1,-1)$

Figure 2.6: Fuzzy Impulse noise detection: Basic and Related gradients.

Besides this algorithms, different approaches based on the median filter, such as the Centered Weighted Median Filter (CWMF) and its modifications, has been widely covered in the literature [27, 24].

Algorithm 1 Fuzzy Impulse noise detection

initialization;
if $\Delta_{basic}I(i,j)$ *is large* ***and*** $\Delta_{related\ 1}I(i,j)$ *is small*
or $\Delta_{basic}I(i,j)$ *is large* ***and*** $\Delta_{related\ 2}I(i,j)$ *is small*
or $\Delta_{basic}I(i,j)$ *is big positive* ***and*** $\Delta_{related\ 1}I(i,j)$ *is big negative* ***and*** $\Delta_{related\ 2}I(i,j)$ *is big negative*
or $\Delta_{basic}I(i,j)$ *is big negative* ***and*** $\Delta_{related\ 1}I(i,j)$ *is big positive* ***and*** $\Delta_{related\ 2}I(i,j)$ *is big positive*
then
    $\Delta^{(F)}I(i,j)$ is large
end
if *most of the* $\Delta^{(F)}I(i,j)$ *are large*
then
    $I(i,j)$ is an Impulse noise pixel
end

2.5 Gaussian Additive Noise Variance Estimation

In [31], a noise variance estimator with a very simple concept and interesting results, which bases on the low variability areas natural images contains, is presented. For the Gaussian Additive noise scenario, the estimator is based on the variances from multiple patches from the entire image. Based on this variance collection, it is proposed to use its mode as an unbiased estimator.

The variance estimation is crucial for the multiple noise scenarios, including the Gaussian Additive scenario, since most of the filtering processes requires the image noise level [5]. Based on an Additive noise scenario:

$$b(x,y) = u(x,y) + \eta(x,y), \tag{2.40}$$

where b is the degraded image (observation), u is the original image, and η is the additive noise, the overall variance can be expressed as:

$$\sigma^2_{b(x,y)} = \sigma^2_{u(x,y)} + \sigma^2_{\eta} \tag{2.41}$$

Where $\sigma^2_{b(x,y)}$, $\sigma^2_{u(x,y)}$ are local variances. So, if $\sigma^2_{u(x,y)} = 0$ (homogenous local region), then $\sigma^2_{b(x,y)} = \sigma^2_{\eta}$. In order to exploit this condition to find the noise level, an homogenous zone selection is required. Assuming an ideal case: $\sigma^2_{\eta} = \sigma^2_{min} = min_{x,y}\{\sigma^2_{b(x,y)}\}$. However, in a real scenario, this estimator is sensitive to outliers. Another common employed estimator is $\sigma^2_{\text{MAD}} = 1.4826 \cdot \text{MAD}(y^H_{ij})$, which is the median absolute deviation of the highest wavelet decomposition stage of a signal, i.e. $\text{MAD}(f) = median(f - median(f))$. Beside the mentioned methods, A wide variety of them is covered in [24].

The effect of adding White Gaussian noise in the sample variances along patches in the image corresponds to a right shift in its distribution, i.e. in its histogram. This reflects in a uniform increase in the observation variance itself. The literature suggests based in this phenomenom that an effective noise estimator based on the population distribution of the variance is the mode. Modeling the noise as a Gaussian distribution and assuming a constant image scenario, it is shown that if we choose

$$\sigma^2_{\eta} = \frac{1}{N}\sum \sigma^2_{b(x,y)}, \tag{2.42}$$

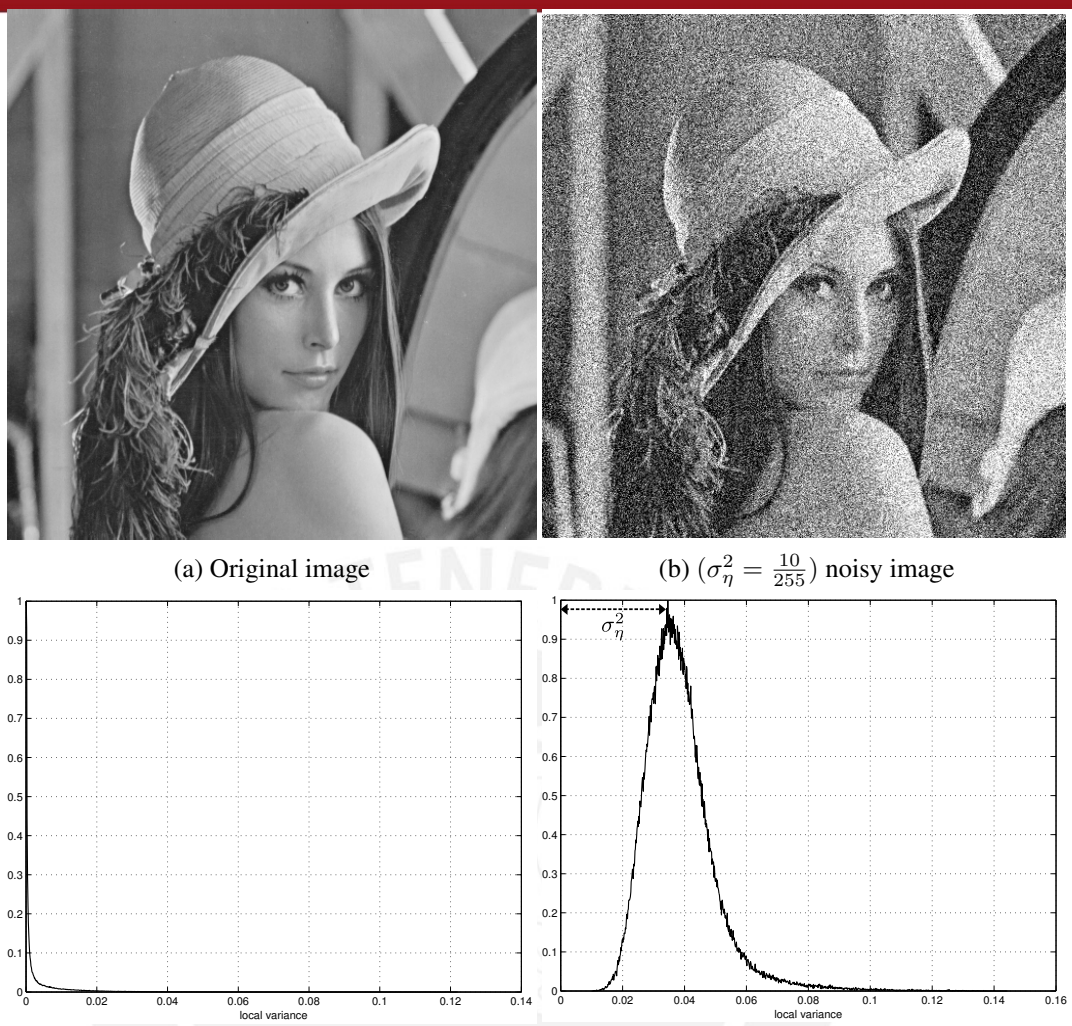

(a) Original image

(b) ($\sigma_\eta^2 = \frac{10}{255}$) noisy image

(c) Original image local variance histogram

(d) Noisy image local variance histogram

Figure 2.7: Gaussian Additive noise estimation by local variance histogram approach.

we obtain the maximum likelihood estimator for σ^2_{sample}. Another estimator which gets close to σ^2_η for N large is $Mode\{\sigma^2_{sample}\}$.

$$Mode\{\sigma^2_{sample}\} = \sigma^2 \frac{N-3}{N-1}, \tag{2.43}$$

$$\frac{N-1}{N-3} Mode\{\sigma^2_{sample}\} = \sigma^2, \tag{2.44}$$

For typical natural images, which mostly contains homogenous zones, the variance distribution has its peak around 0. Analyzing the distributions of a test picture set and approximating them to known statistical models, it is shown that, depending on the variability ratio between image and noise, the mode is not the actual Maximum likelihood σ^2_η estimation, however it approximates to it. Figure 2.7 shows the noise variance estimation for a natural image and its Gaussian Additive noise corrupted counterpart based on their variances histogram.

Chapter 3

Proposed Restoration Framework

Given the previous concepts, a ℓ^1 plus ℓ^2 Total Variation formulation capable of restoring images under Impulse over Gaussian Additive noise is introduced, and an optimal regularization parameter estimation framework is proposed. Additionally, the framework focuses also on the Impulse noise scenario as a particular case of the Impulse over Gaussian Additive case. Regarding the Gaussian Additive noise scenario, since the proposed framework includes the UPRE, which remarkable performance for the Gaussian Additive noise scenario has already been covered in the literature (refer to [17, 4] for more details), the proposed framework does not focus on this noise model.

For a non-mixed noise model like the Gaussian Additive or Impulse scenario, there are several methods that successfully estimate the corrupted pixel set and noise level such as those mentioned in Section 2. However, none of this methods covers the scenario where more than a single noise model is present. Furthermore, the classic Total Variation cost function parameters are selected focusing on single noise models. Finally, a well conditioned metric is required in order to define an optimal regularization parameter. In the following, this requirements are analyzed in detail in order to propose a method that encompasses them. Also, the framework proposed in [1, 4] is revisited in order to extend such concepts to a general denoising procedure.

3.1 Salt and Pepper Noise Scenario Approach: Spatially Adaptive Iteratively Reweighted Norm

An image restoration method for the Salt and Pepper noise model is stated in the preliminary work published in [1], which uses a modification on the ℓ^1 TV functional. By taking advantage of the ℓ^1 TV functional benefits for this noise model shown in [14, 19], the proposed approach consists on applying a local fashioned ℓ^1 TV regularization on an estimated noise set obtained by a two-phase filter. The following section describes its framework.

3.1.1 Iteratively Reweighted Norm Algorithm

The Iteratively Reweighted Norm (IRN) algorithm [21, 32] is a computationally efficient and flexible Total Variation minimization method for grayscale and color images that can

handle the $p > 0$ and $q \leq 2$ norms in the regularization and fidelity terms, respectively. This includes the ℓ^2-TV and ℓ^1-TV as special cases. The algorithm attacks the minimization problem basing on the Iteratively Reweighted Least Squares (IRLS) approach [33], i.e. by representing the ℓ^p and ℓ^q norms by their equivalent weighted ℓ^2 norms in an iterative fashion. Given the IRLS method, the cost function

$$\frac{1}{r}||\mathbf{u}||_r^r = \frac{1}{r}\sum_i |u_i|^r, \tag{3.1}$$

can be iteratively approaximated by

$$\frac{1}{2}||W^{1/2}\mathbf{u}||_2^2 = \frac{1}{2}\mathbf{u}^T W\mathbf{u} = \frac{1}{2}\sum_i w_i u_i^2, \tag{3.2}$$

where

$$W = \frac{2}{r}\,\mathrm{diag}(|\mathbf{u}|^{r-2}), \tag{3.3}$$

which is estimated iteratively by using the cost function minimizer from the previous iteration ($\mathbf{u}$).

Following this, the IRN approach, which converges to the solution of (2.13), is expressed as:

$$\min_{\mathbf{u}}\ T^{(k)}(\mathbf{u}) = \frac{1}{2}\left\|W_F^{(k)^{1/2}}(\mathbf{u}-\mathbf{b})\right\|_2^2 + \frac{\lambda}{2}\left\|W_R^{(k)^{1/2}}D\mathbf{u}\right\|_2^2, \tag{3.4}$$

where

$$W_F^{(k)} = \mathrm{diag}\left(\tau_{F,\epsilon_F}(\mathbf{u}^{(k)}-\mathbf{b})\right), \tag{3.5}$$

$$W_R^{(k)} = I_{2L}\otimes\Omega^{(k)}, \tag{3.6}$$

$$\Omega^{(k)} = \mathrm{diag}\left(\tau_{R,\epsilon_R}\left(\sum_{n\in C}(D_x\mathbf{u}_n^{(k)})^2 + (D_y\mathbf{u}_n^{(k)})^2\right)\right), \tag{3.7}$$

$$\tau_{F,\epsilon_F}(x) = \begin{cases} |x|^{p-2} & \text{if } |x| > \epsilon_F \\ \epsilon_F^{p-2} & \text{if } |x| \leq \epsilon_F \end{cases}, \tag{3.8}$$

$$\tau_{R,\epsilon_R}(x) = \begin{cases} |x|^{(q-2)/2} & \text{if } |x| > \epsilon_R \\ 0 & \text{if } |x| \leq \epsilon_R \end{cases}, \tag{3.9}$$

$$D = I_L \otimes [Dx^T\, Dy^T]^T, \tag{3.10}$$

I_L is an $L\times L$ identity matrix, $\otimes$ is the Kronecker product, and L is a scalar which depends on the image layers (typically, $L = 1$ for $C = \{1\}$, or $L = 3$ for $C = \{1, 2, 3\}$. Following a common strategy in IRLS type algorithms, the functions $\tau_{F,\epsilon_F}(x)$ and $\tau_{R,\epsilon_R}(x)$ are defined

to avoid numerical problems when $\mathbf{u}^{(k)} - \mathbf{b}$ or $\sum_{n \in C} (D_x \mathbf{u}_n^{(k)})^2 + (D_y \mathbf{u}_n^{(k)})^2$ has zero-valued components.

3.1.2 Local Regularization

A Total Variation cost function modification is proposed. This new cost function of interest is the modified ℓ^1-TV problem:

$$\min_{\mathbf{u}} \; T(\mathbf{u}) = \left\| \Lambda^{-1}(\mathbf{u} - \mathbf{b}) \right\|_1 + \left\| \sqrt{\sum_{n \in C} (D_x \mathbf{u}_n)^2 + (D_y \mathbf{u}_n)^2} \right\|_1, \tag{3.11}$$

It is straighforward to check that if Λ is fixed, the IRN algorithm can be used to solve (3.11). The equivalent weighted ℓ^2 version of the modified ℓ^1-TV problem can be written as:

$$\min_{\mathbf{u}} \; T^{(k)}(\mathbf{u}) = \frac{1}{2} \left\| W_F^{(k)^{1/2}} \Lambda^{(k)^{-1/2}} (\mathbf{u} - \mathbf{b}) \right\|_2^2 + \frac{1}{2} \left\| W_R^{(k)^{1/2}} D\mathbf{u} \right\|_2^2, \tag{3.12}$$

where $\Lambda^{(k)} > 0$ is a diagonal matrix defined in some fashion. Since (3.12) is quadratic and its Hessian $\nabla^2 T^{(k)}(\mathbf{u}) = \left(W_F^{(k)} \Lambda^{(k)^{-1}} + D^T W_R^{(k)} D \right)$ is greater than zero, then the minimum of (2.13) can be reached by iteratively solving

$$\left(W_F^{(k)} \Lambda^{(k)^{-1}} + D^T W_R^{(k)} D \right) \mathbf{u} = W_F^{(k)} \Lambda^{(k)^{-1}} \mathbf{b}. \tag{3.13}$$

By replacing a scalar parameter by a vector, it is shown that the new Total Variation solution is capable of penalizing each pixel in a particular way [1]. Given this new feature, the way Total Variation fits to noise models acquires more flexibility, and thus allows better reconstruction results for more complex noise models. By approximating this new cost function to ℓ^2 norms by applying the Iteratively Reweighted Norm algorithm, the result is a Spatially Adaptive IRN algorithm (SAIRN). Algorithm 2 presents the resulting method.

3.1.3 Salt and Pepper Noise Estimation

The Salt and Pepper noise detector based on the adaptive median filter described in (2.4.1) is used for the outliers detection. The proposed algorithm defines the set W, which is zero if the element l is noise-free and w_n^l if it is noisy. This gives information about the local noise level for each noise-corrupted pixel. Note that the global noise level p can be estimated as $\tilde{p} = \frac{1}{N} \sum \mathbf{I}_{[W \neq 0]}$, where N is the number of pixels and I is the indicator function.

3.1.4 Parameter Update

In [34], an estimation of local statistics for a fixed, manually selected neighborhood size is applied in order to give a hint about the noise level of the residual ($\mathbf{r} = \mathbf{u} - \mathbf{b}$) along with a rule based procedure to spatially update the regularization parameter. The SAIRN algorithm also makes use of local statistics of the residual, but based on particular neighborhood sizes.

Algorithm 2 Spatially Adaptive IRN algorithm for ℓ^1-TV

Initialize

Estimate set W from $\mathbf{b}$

$\Lambda^{(0)} = \text{diag}(\mathbf{I}_{[w_n^l(l)>0]}) + 10^{-6}\,\text{diag}(\mathbf{I}_{[w_n^l(l)==0]})$

$\mathbf{u}^{(0,0)} = \left(I + \Lambda^{(0)} D^T D\right)^{-1} \mathbf{b}$

for $m = 0, 1, .., \mathbf{M}$

for $k = 1, 2, .., \mathbf{K}$

$W_F^{(k)} = \text{diag}\left(\tau_{F,\epsilon_F}(\mathbf{u}^{(m,k-1)} - \mathbf{b})\right)$ for $p = 1$

$\Omega_R^{(k)} = \text{diag}\left(\tau_{R,\epsilon_R}\left((D_x\mathbf{u}^{(m,k-1)})^2 + (D_y\mathbf{u}^{(m,k-1)})^2\right)\right)$ for $q = 1$

$W_R^{(k)} = \begin{pmatrix} \Omega_R^{(k)} & 0 \\ 0 & \Omega_R^{(k)} \end{pmatrix}$

$\mathbf{u}^{(m,k)} = \left(I + \Lambda^{(m)} {W_F^{(k)}}^{-1} D^T W_R^{(k)} D\right) \mathbf{b}$

end

$\mathbf{r} = \mathbf{u}^{(m,\mathrm{K})} - \mathbf{b}$

estimate $\hat{\mathbf{p}}$ (via (3.14))

compute $\Lambda^{(m+1)}$ (via (3.15))

end

The local noise estimator is defined as:

$$\hat{p}_n(l) = \frac{1}{M} \sum_{k \in \mathcal{K}_{w_n^l}(l)} |r_n(l)| \tag{3.14}$$

where $M = (2 \cdot w_n^l + 1)^2$ and $\mathcal{K}_{w_n^l}(l)$ is defined as in (2.4.1). The spatially dependant regularization parameter Λ is initialized as $\Lambda^{(0)} = \text{diag}(\boldsymbol{\lambda}^{(0)})$, with $\lambda^{(0)}(l) = \text{diag}(\mathbf{I}_{[w_n^l(l)>0]}) + 10^{-6}\,\text{diag}(\mathbf{I}_{[w_n^l(l)==0]})$. After solving (3.11), $\hat{p}_n(l)$ is computed in order to obtain the regularization parameter updates $\lambda_n^{(m)}(l)$ in a spatially dependant fashion:

$$\lambda_n^{(m)}(l) = \begin{cases} \rho^{-1} \cdot \lambda_n^{(m-1)}(l) & \text{if } \hat{p}_n(l) < \tilde{p} \cdot \sigma \\ \rho \cdot \lambda_n^{(m-1)}(l) & \text{if } \hat{p}_n(l) > \tilde{p} \cdot \sigma \end{cases}, \tag{3.15}$$

where ρ, σ are constant values and $\tilde{p}$ is the estimated global noise level.

The SAIRN focuses on the Salt and Pepper noise scenario. As an initial step, it uses the RAMF as an Impulse noise detector. Following this, an initial $(\Lambda^{(0)})$ is defined to start the IRN iterations. at each step, $(\Lambda^{(k)})$ is updated according the remaining noise in $(\mathbf{r} = |\mathbf{b} - \mathbf{u}^{(\mathbf{k})}|)$.

3.1.5 Regularization Parameter Selection without Update Strategy

Since it is possible to estimate the Impulse noise pixel set, the restoration problem for such a noise model becomes a local Total Variation problem. The use of the SAIRN under this scenario has shown to give promising results for a wide noise level range. Moreover, the

local approach it uses can be modeled as a variational method generalization for low noise level cases, since it is capable of restricting its penalization areas based on the estimated noise set without neglecting the noise free elements. Consequently, a new adaptive scheme was proposed as a preliminary stage for this work with a considerable change in the update criteria, which has proven to get a faster convergence rate [4].

For the ℓ^1 TV image denoising under Impulse noise scenario, the elementwise Total Variation solution for a particular (λ) is given by the following:

$$u_{(i,j,\lambda=0)} = b(i) \tag{3.16}$$

$$u_{(i,j,\lambda\to\infty)} = \frac{u_{(i+1,j)} + u_{(i,j+1)}}{2}, \tag{3.17}$$

for a forward operator based finite differentiation and the anisotropic Total Variation model. Hence, local solutions lie between the observation pixel value ($b_{(i,j)}$) and a pixel-based average which bases on its neighborhood intensity values ($\frac{u_{(i+1,j)}+u_{(i,j+1)}}{2}$).

Following the arguments stated in [31], the information of a natural image is contained in its edges and form coherent structures of homogeneous regions. This means that most of the noise pixels, except the ones located close to edges and other features, have an original intensity which is very close to its neighborhood. On the other hand, as mentioned in Section 2, Impulse noise pixels holds no information about their real intensity.

Figure 3.1 shows noise pixels for three different image regions on the ($s = 0.05$) Impulse corrupted (gray) Lena: An edge region, a flat region, and a noise cluster region. In addition, Figure 3.2 presents the λ impact for such structures, based on the absolute difference between the original and reconstructed intensities. The λ search shows how the edge region reaches an accurate reconstruction inside the range defined by $b_{(i,j)}$ and $\frac{u_{(i+1,j)}+u_{(i,j+1)}}{2}$. On the other hand, the flat region and the noise cluster reach good estimates which tend to $\frac{u_{(i+1,j)}+u_{(i,j+1)}}{2}$. This behavior is coherent with the previous argument for flat regions. For the edge region and noise cluster, the optimal λ may depend on how big is the intensity range defined by $[b_{(i,j)}; \frac{u_{(i+1,j)}+u_{(i,j+1)}}{2}]$.

Based on this, it is proposed to minimize the Total Variation fidelity term impact on the noise pixel set, which reflects in a Λ with big valued elements. This forces a noise pixel set solution based purely on their neighbors values. This implies no loss of certainty, since Impulse noise pixels holds no original information. On the other hand, since Λ penalizes only the noise pixel set, the Total Variation regularization term for the noise free pixels is minimized, so they remain unaltered. This argument can also be applied to the isotropic representation of the Total Variation term, since it also depends on its neighbors.

Finally, the optimal Total Variation solution is defined by solving the IRN scheme:

$$\left(W_F^{(k)}{\Lambda^{(k)}}^{-1} + D^T W_R^{(k)} D\right)\mathbf{u} = W_F^{(k)}{\Lambda^{(k)}}^{-1}\mathbf{b}. \tag{3.18}$$

for u. the SAIRN defines Λ as $diag(\frac{1}{\lambda_0}, ..., \frac{1}{\lambda_{n-1}})$ for $b \in \mathbb{R}^n$. Then, following the new criteria, let

$$\lambda_i = \begin{cases} 0 & ,i \notin \mathcal{N} \\ c >> 1 & ,i \in \mathcal{N} \end{cases} \tag{3.19}$$

Figure 3.3 shows the reconstruction quality (PSNR) contrast between the adaptive λ iterative scheme, with $\rho = 0.75$ and $\sigma = 0.5$, and the fixed λ iterative scheme for grayscale Lena under the Impulse noise scenario $(s = 0.25)$. Convergence for the fixed scheme considerably increases, while the quality remains almost the same without the need of updating Λ.

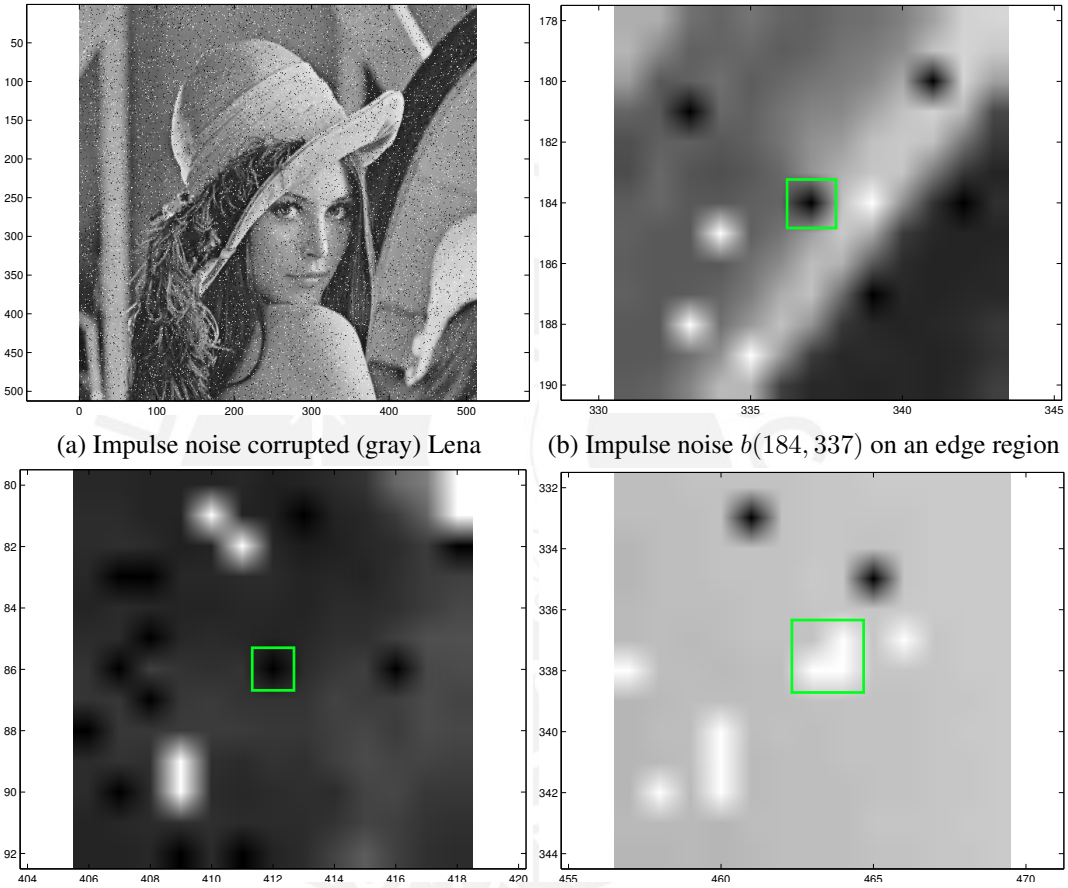

(a) Impulse noise corrupted (gray) Lena

(b) Impulse noise $b(184, 337)$ on an edge region

(c) Impulse noise $b(86, 412)$ on an flat region

(d) Impulse noise cluster region

Figure 3.1: Image structure regions for the Impulse noise scenario.

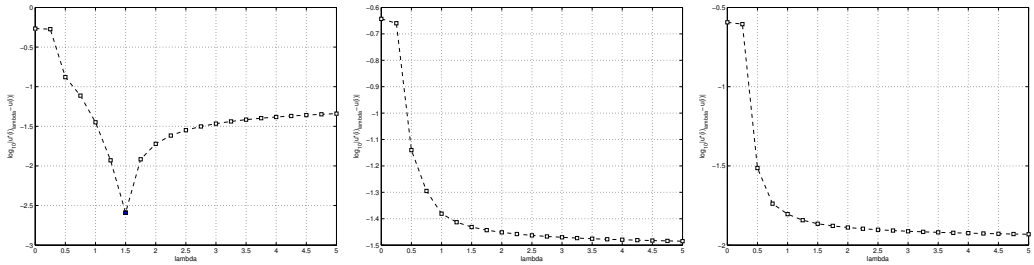

(a) $b(184, 337)$ λ response

(b) $b(86, 412)$ λ response

(c) Noise cluster λ response

Figure 3.2: Optimal local regularization parameter grid search behavior for different image structures for the Impulse noise scenario.

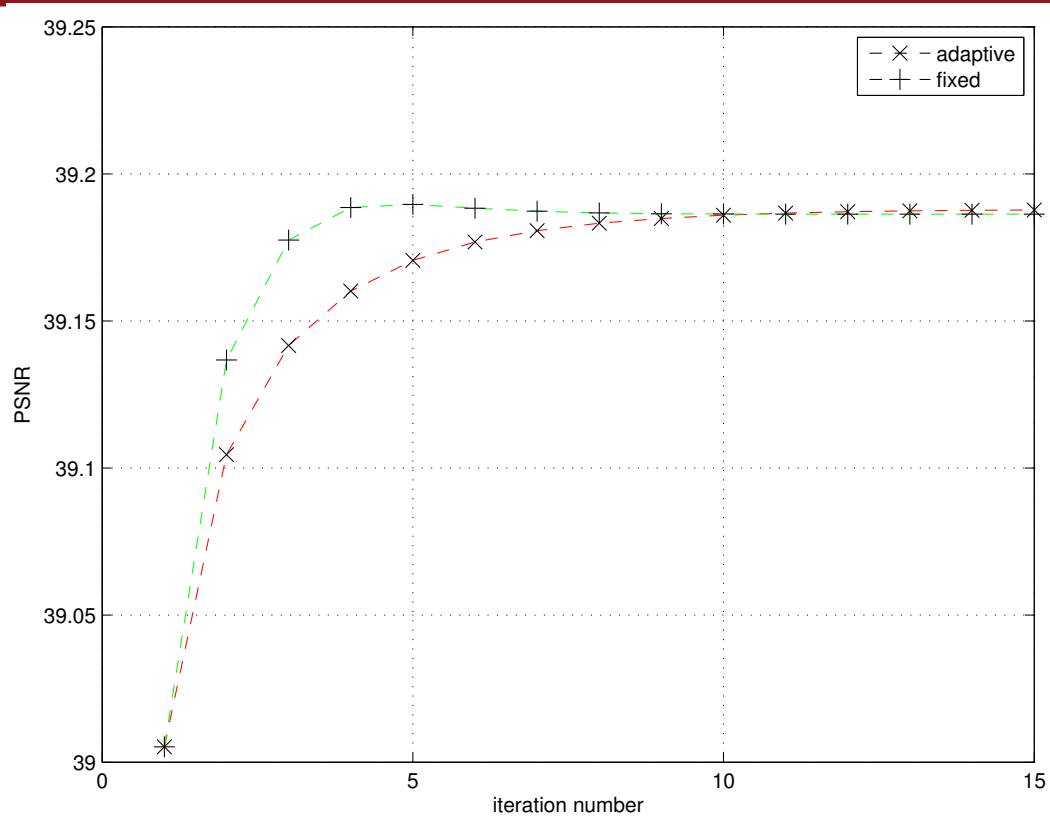

Figure 3.3: Iterative fixed approach versus Iterative adaptive scheme (with $\rho = 0.65$ and $\sigma = 0.5$) quality contrast for (gray) Lena under the Impulse noise scenario ($s = 0.25$).

3.2 Impulse over Gaussian Additive Noise Scenario Approach: Modified Spatially Adaptive Iteratively Reweighted Norm

The SAIRN achieves high quality results for the Salt and Pepper noise scenario because, with high probability, the ℓ^1 Total Variation solution derives from noise free image elements. For relatively low noise corruption levels, most of the Impulse noise corrupted elements' neighborhood belongs to noise free elements. Under these circumstances, The use of either statistical filters or variational methods, such as the RAMF and ℓ^1 Total Variation respectively, have proven to give good results [5]. For relatively high noise corruption levels, corrupted pixel clusters appears. In contrast to the former case, filtering under this conditions attains poor quality results since the output for each element depends on its corrupted neighbors. Given this scenario, SAIRN iterative approach leads to a progressive cluster shrinkage. Due to the fact that some of the elements within a cluster, those in the cluster edges, have uncorrupted elements within their neighborhood, the ℓ^1 Total Variation output they attain is based on trusty information, and so it can be seen as an accurate interpolation. Then, the iterative behavior can be seen as a chain interpolation: a set of corrupted elements within a cluster finds a stable solution at each iteration, giving accurate information to the rest of elements within the cluster. This scheme is kept until the entire cluster finds an unfluctuating solution.

For an Impulse over Gaussian Additive noise scenario, the mentioned scheme is un-

able to attain high quality outputs because the entire image is distorted. Any attempt of reconstructing the Impulse noise pixels based on whether filtering or variational methods derives from corrupted elements. Furthermore, the SAIRN algorithm targets only the Impulse noise, leaving the Gaussian Additive noise behind. Based on this limitations, a novel iterative scheme is proposed based on the SAIRN procedure. However, consistent modifications are done in order to surpass this new scenario.

A ℓ^1 plus ℓ^2 locally regularized Total Variation reconstruction is proposed for this Mixed noise model. This means two separate reconstructions: a ℓ^1 TV reconstruction for the Impulse noise pixel set and a ℓ^2 TV reconstruction for the Gaussian Additive noise pixel set. In addition to the already stated SAIRN framework, a noise set estimation which discriminates between both models and an accurate criteria for choosing the optimal regularization parameter for the ℓ^2 TV reconstruction is required. Furthermore, since both separate reconstructions derives directly from corrupted pixels, a decision must be made in order to choose which noise model must be dealt with first.

3.2.1 Impulse Noise: Outliers Detection

For this Mixed noise scenario, it is still possible to recognize the Impulse corrupted pixel set $\mathcal{N}$, since they are still represented as outliers. Of course, this also implies the identification of the Additive corrupted pixel set. However, experimental results show that the RAMF accuracy descreases considerably, specially under high Gaussian Additive noise level. The proposed scheme uses two different observations in order to obtain a more accurate estimation of $\mathcal{N}$. The DWMF and the RAMF observations are combined in order define estimate the corrupted set. So, let $\mathcal{N}_{\text{DWMF}}$ denote the element set defined as Noise by the DWMF, i.e.

$$min\{d_{i,j}^{(k)}\} > T_d : 1 \leq k \leq 4, \tag{3.20}$$

And $\mathcal{N}$ the element set defined as noise by the RAMF, i.e.

$$\mathcal{N}_{\text{RAMF}} : \{n \in C, l \in \Omega : \hat{b}_n^{w_n^l}(l) \neq b_n(l) \wedge b_n(l) \in \{\text{v}_{min},\ \text{v}_{max}\}\}, \tag{3.21}$$

Then, the estimated Impulse noise set is defined as

$$\mathcal{N} : \mathcal{N}_{\text{RAMF}} \cap \mathcal{N}_{\text{DWMF}} \tag{3.22}$$

Following this, the Gaussian Additive noise corrupted set can be defined as

$$\mathcal{G} : \Omega \setminus \mathcal{N} \tag{3.23}$$

3.2.2 Gaussian Additive Noise: Local Risk Estimation

The selection of which set $(\mathcal{G}, \mathcal{N})$ must be approached first is crucial in the procedure. As mentioned before, the Impulse noise pixels hold no information about its original intensities. On the other hand, Additive noise corrupted elements does hold information.

It is proposed to find a solution for the Impulse corrupted element set based on $\mathcal{N}_{\text{RAMF}} \cap \mathcal{N}_{\text{DWMF}}$ as an initial step. Since, ideally, only the Impulse noise corrupted pixels are modified, the Gaussian Additive noise elements suffer no information loss.

After this step, the resulting image is formed by the Gaussian Additive noise pixels and their interpolation which replaces the Impulse noise pixels. This new image cannot be taken as a plain Gaussian Additive noise scenario, even when no outliers remain, for two main reasons: First, the interpolation does not holds any information about the original Impulse noise pixels. Second, applying this scheme may modify the noise properties due to the fact that new intensities in different proportions are being introduced to the new image. That is, if there was an initial Additive noise distribution affecting the original image, then the resulting image does not hold it.

The purpose of creating this intermediate output is to find an Additive corrupted element set Total Variation solution based on coherent non-outlier intensities. This is similar to the plain Impulse noise case, where the Impulse pixel set find new intensities based noise free elements only. However, in this new scenario, the only pixels holding true information are the Additive noise elements. So, an iterative procedure first regularizes $\mathcal{N}$ based on the Additive noise elements in order obtain structure-coherent intensities, and then regularizes $\mathcal{G}$ based on this new intensities.

By using the UPRE, an accurate ℓ^2 TV reconstruction for the Gaussian Additive noise scenario may be achieved by searching for the optimal regularization parameter as the risk minimizer in the λ space [9]. However, under a Mixed noise scenario, the UPRE method needs to be modified as a local operator so that it performs over a specific pixel set and not the entire image. In the following, we introduce a UPRE modification in order to apply it in a local fashion.

Let $\text{MSE}^{(g)} = \text{MSE}(u_\lambda^{(g)})$ denote the mean square error of the estimated Gaussian corrupted elements set. This risk measurement tells the error between the original and the restored elements in $\mathcal{G}$ by a specific λ. In order to estimate the risk measurement, i.e. the UPRE for this set, then it must only take into account the elements in $\mathcal{G}$. Let $W_g = \text{diag}(w_0, ..., w_{n-1})$, where

$$w_i = \begin{cases} 0 & ,i \notin \mathcal{G} \\ 1 & ,i \in \mathcal{G} \end{cases}$$

then, using this mask into the UPRE calculation:

$$\text{UPRE}^{(g)} = \frac{\|W_g r_\lambda\|}{|\mathcal{G}|} + \frac{\hat{\sigma}_\eta^2}{|\mathcal{G}|}\text{Trace}(W_g A(u_\lambda)) - \hat{\sigma}_\eta^2 \tag{3.24}$$

An important detail is that, since the UPRE is applied to a portion of the image, then $\hat{\sigma}^2$ should take into account just the elements belonging to $\mathcal{G}$. This is accomplished by taking into account only the very same elements when estimating the noise variance.

Regarding the Hutchinson estimate used for calculating the UPRE, the shown modifi-

cation is reflected as:

$$r = v^T W_g (K(K^T K + \lambda L(u_\lambda))^{-1} K^T) v \tag{3.25}$$

or

$$r = v_0^T (K^T K + \lambda L(u_\lambda))^{-1} v_1 \tag{3.26}$$

where $v_0 = K^T W_g v$ and $v_1 = K^T v$. So, the requirement of a solver for $(K^T K + \lambda L(u_\lambda))r = v_1$ is kept.

Given this modification, a Golden search on the λ space is proposed to find the UPRE minimizer and estimate the optimal regularization parameter for the local ℓ^2 TV reconstruction.

3.2.3 Modified Spatially Adaptive Iteratively Reweighted Norm

Once the Additive noise corrupted elements are restored, the Impulse noise corrupted elements should follow. Since the set $\mathcal{G}$ intensities are now closer to their original values, an intuitive approach is to apply the SAIRN scheme to this pre-denoised image. Given the attenuated Additive noise, the Impulse noise elements reconstruction should give more accurate results. Algorithm 3 shows the proposed method.

Algorithm 3 Modified Spatially Adaptive Iteratively Reweighted Norm for the Impulse over Gaussian Additive noise scenario

Initialize

Estimate $\mathcal{N}$: $\mathcal{N}_{\text{RAMF}} \cap \mathcal{N}_{\text{DWMF}}$ from $\mathbf{b}$

Estimate $\mathcal{G}$: $\Omega \setminus \mathcal{N}$ from $\mathbf{b}$

$\Lambda_i = \lambda_0 \operatorname{diag}(\mathrm{I}_{[i\in\mathcal{N}]}) + \epsilon \operatorname{diag}(\mathrm{I}_{[i\notin\mathcal{N}]}), \quad \lambda_0 >> 1, \quad \epsilon \in \mathbb{R}^+ << 1$

$\mathbf{u}^{(0)} = \left(I + \Lambda_i D^T D\right)^{-1} \mathbf{b}$

`// Solve local` ℓ^1 `TV for` $\mathbf{b}$

for $k = 1, 2, .., \mathbf{K}$

$W_F^{(k)} = \operatorname{diag}\left(\tau_{F,\epsilon_F}(\mathbf{u}^{(k-1)} - \mathbf{b})\right)$ for $p = 1$

$\Omega_R^{(k)} = \operatorname{diag}\left(\tau_{R,\epsilon_R}\left((D_x\mathbf{u}^{(k-1)})^2 + (D_y\mathbf{u}^{(k-1)})^2\right)\right)$ for $q = 1$

$W_R^{(k)} = \begin{pmatrix} \Omega_R^{(k)} & 0 \\ 0 & \Omega_R^{(k)} \end{pmatrix}$

$\mathbf{u}^{(k)} = \left(I + \Lambda_i {W_F^{(k)}}^{-1} D^T W_R^{(k)} D\right) \mathbf{b}$

end

Calculate $\lambda^* = \arg\min_\lambda \text{UPRE}_{TV,\lambda}^{(g)}(\mathbf{u}^{(\mathbf{K})})$

$\Lambda_g = \lambda^* \operatorname{diag}(\mathrm{I}_{[i\in\mathcal{G}]}) + \epsilon \operatorname{diag}(\mathrm{I}_{[i\notin\mathcal{G}]})$

$\mathbf{v}^{(0)} = \left(I + \Lambda_g D^T D\right)^{-1} \mathbf{u}^{(\mathbf{K})}$

`// Solve local` ℓ^2 `TV for` $\mathbf{u}$

for $m = 1, 2, .., \mathbf{M}$

$W_F^{(m)} = \operatorname{diag}\left(\tau_{F,\epsilon_F}(\mathbf{v}^{(m-1)} - \mathbf{u}^{(\mathbf{K})})\right)$ for $p = 2$

$\Omega_R^{(m)} = \operatorname{diag}\left(\tau_{R,\epsilon_R}\left((D_x\mathbf{v}^{(m-1)})^2 + (D_y\mathbf{v}^{(m-1)})^2\right)\right)$ for $q = 1$

$W_R^{(m)} = \begin{pmatrix} \Omega_R^{(m)} & 0 \\ 0 & \Omega_R^{(m)} \end{pmatrix}$

$\mathbf{v}^{(m)} = \left(I + \Lambda_g {W_F^{(m)}}^{-1} D^T W_R^{(m)} D\right) \mathbf{u}^{(\mathbf{K})}$

end

$\mathbf{w}^{(0)} = \left(I + \Lambda_i D^T D\right)^{-1} \mathbf{v}^{(\mathbf{M})}$

`// Solve local` ℓ^1 `TV for` $\mathbf{w}$

for $k = 1, 2, .., \mathbf{K}$

$W_F^{(k)} = \operatorname{diag}\left(\tau_{F,\epsilon_F}(\mathbf{w}^{(k-1)} - \mathbf{v}^{(\mathbf{M})})\right)$ for $p = 1$

$\Omega_R^{(k)} = \operatorname{diag}\left(\tau_{R,\epsilon_R}\left((D_x\mathbf{w}^{(k-1)})^2 + (D_y\mathbf{w}^{(k-1)})^2\right)\right)$ for $q = 1$

$W_R^{(k)} = \begin{pmatrix} \Omega_R^{(k)} & 0 \\ 0 & \Omega_R^{(k)} \end{pmatrix}$

$\mathbf{w}^{(k)} = \left(I + \Lambda_i {W_F^{(k)}}^{-1} D^T W_R^{(k)} D\right) \mathbf{v}^{(\mathbf{M})}$

end

Chapter 4

Experimental Results

The proposed framework is evaluated under Impulse noise and Impulse over Gaussian Additive noise, as depicted in Section 3. A contrast between the present work and the results reported on [2, 21, 32] and [35, 3, 4] is elaborated in order to show its performance against the state of the art algorithms. Each algorithm in the proposed framework is evaluated under different noise conditions against the state of the art algorithms. Furthermore, an evaluation on the SAIRN update scheme parameters $(\rho; \sigma)$ reconstruction quality impact for the Impulse noise scenario is included. The evaluated quality metrics are the following:

$$\text{SNR}\big(10\log_{10}\frac{\text{N}\sigma^2\{\mathbf{u}^*\}}{\|\mathbf{u}-\mathbf{u}^*\|_2^2}\big),$$

$$\text{PSNR}\big(10\log_{10}\frac{\text{N}(\max\{\mathbf{u}\})^2}{\|\mathbf{u}-\mathbf{u}^*\|_2^2}\big),$$

and SSIM [36], where N is the number of pixels in all the image layers. The simulations are carried out using Matlab code on a 3GHz. Intel core i7 processor (1024KB. L2 Cache, 4GB. RAM).

4.1 Spatially Adaptive Iteratively Reweighted Norm: Update Scheme Parameters Evaluation

The output for different SAIRN update parameter values (ρ; σ) is presented in order to show their reconstruction quality impact. Figures (4.11 - 4.13) show the quality results for (gray) Lena, (gray) Peppers and (gray) Bridge; for $s = \{5\%; 25\%; 75\%\}$, σ in the range of $[0.25 - 1.25]$ (steps of 0.5) and ρ in the range of $[0.6 - 5.0]$.

Regarding ρ, while the curves does not show an optimal value, $\rho = 0.6$ and $\rho = 0.7$ show the best reconstruction quality for (gray) Lena and (gray) Peppers in most s and ρ scenarios. On the other hand, covered σ values show no considerable impact for $s = \{25\%; 75\%\}$ on the image test set. However, for $s = 5\%$, $\rho = 1.25$ shows a slight reconstruction quality increase for (gray) Lena and (gray) Bridge, while a slight decrease for (gray) Peppers. Finally, results also show how $\rho > 1$ has an unfavorable impact in the reconstruction quality, which keep the same reconstruction quality along all the iterations.

$\hat{\sigma}_\eta^2$	MSE_{grid}		$\text{UPRE}_{\text{grid,tr. comp.}}$		$\text{UPRE}_{\text{grid,tr. est.}}$		$\text{UPRE}_{\text{golden,tr. est.}}$	
	$64^2px.$	$128^2px.$	$64^2px.$	$128^2px.$	$64^2px.$	$128^2px.$	$64^2px.$	$128^2px.$
$\frac{10}{255}$	0.01	0.01	0.01	0.01	0.01	0.01	0.0121	0.0122
$\frac{20}{255}$	0.025	0.025	0.03	0.025	0.03	0.03	0.0243	0.0319
$\frac{30}{255}$	0.045	0.04	0.045	0.04	0.045	0.05	0.0441	0.0441
$\frac{40}{255}$	0.06	0.06	0.07	0.06	0.07	0.075	0.0592	0.0714
$\frac{50}{255}$	0.075	0.08	0.08	0.08	0.075	0.09	0.0789	0.0911

Table 4.1: UPRE_{TV} accuracy: λ^* for the computation and estimation of Trace(A_{TV}). MSE_{grid}: MSE grid search; $\text{UPRE}_{\text{grid, tr.comp.}}$: UPRE grid search by Trace(A_{TV}) computation; $\text{UPRE}_{\text{grid, tr.est.}}$: UPRE grid search by Trace(A_{TV}) estimation; $\text{UPRE}_{\text{golden, tr.est.}}$: UPRE golden Search by Trace(A_{TV}) estimation.

Although the proposed framework does not include the SAIRN iterative (Λ) update scheme, the evaluation shows how, under different scenarios, there may not be optimal ρ and σ values. Instead, for images with different features and structural characteristics, such parameters may be specifically selected in order to obtain the best outcome.

4.2 Gaussian Additive Noise Risk Estimation Performance

UPRE computation implies a great cost since it depends upon the Trace(A_{TV}) computation. A_{TV} considerably increases its dimensions for a relatively big observation, which means a serious obstacle. As mentioned in Section 3, the present work uses an alternative approach which does not calculate Trace(A_{TV}). Instead, it uses the Hutchinson Trace Estimator [9], which dramatically reduces the computational requirements. On the other hand, the proposed method estimates λ^* as the UPRE minimizer by searching in the λ space, which requires the ℓ^2 TV calculation for several λ values. Following this, an evaluation of both methods, UPRE computation vs. Hutchinson estimation, for the White Gaussian Noise scenario is presented. Additionally, a Grid search and a Golden search for the λ^* estimation is applied. The accuracy of both methods regarding the Trace(A_{TV}) is analyzed on two patches of (64 x 64) and (128 x 128) pixels on (gray) Lena corrupted by White Gaussian noise with σ_η^2 in the range of [$\frac{10}{255} - \frac{50}{255}$] (steps of $\frac{10}{255}$). Table 4.1 presents the achieved λ^* for each case. Since the test does not include processing time, it is important to remark that the Trace(A_{TV}) calculation time is around fifteen times the time required by the Hutchinson trace estimation in all the evaluations. Despite this, both risk outputs are relatively close.

Finally, the Local UPRE proposed in Section 3 is evaluated for the Impulse over Gaussian Additive noise scenario. A 50% $(s = 0.5)$ Salt and Pepper noise corruption is applied, which in theory leaves half the pixel set corrupted only by Gaussian Additive noise $(\mathcal{G})$. Following this, the Local UPRE should estimate the risk for the Additive noise corrupted elements only. Table 4.2 presents the achieved λ^* for each case. Figure 4.1 shows the λ^* grid search for both patch sizes $(\sigma_\eta^2 = \frac{50}{255})$.

$\hat{\sigma}_\eta^2$	MSE_{grid}		$\text{UPRE}_{\text{grid,tr. comp.}}$		$\text{UPRE}_{\text{grid,tr. est.}}$		$\text{UPRE}_{\text{golden,tr. est.}}$	
	$64^2px.$	$128^2px.$	$64^2px.$	$128^2px.$	$64^2px.$	$128^2px.$	$64^2px.$	$128^2px.$
$\frac{10}{255}$	0.01	0.01	0.015	0.01	0.015	0.01	0.0047	0.0122
$\frac{20}{255}$	0.02	0.025	0.02	0.025	0.02	0.025	0.0244	0.0244
$\frac{30}{255}$	0.035	0.03	0.025	0.03	0.025	0.03	0.0319	0.0441
$\frac{40}{255}$	0.05	0.05	0.04	0.05	0.04	0.05	0.0441	0.0592
$\frac{50}{255}$	0.065	0.07	0.045	0.075	0.045	0.06	0.0714	0.0811

Table 4.2: Local UPRE_{TV} accuracy: λ^* for the computation and estimation of $\text{Trace}(A_{\text{TV}})$. MSE_{grid}: MSE grid search; $\text{UPRE}_{\text{grid, tr.comp.}}$: UPRE grid search by $\text{Trace}(A_{\text{TV}})$ computation; $\text{UPRE}_{\text{grid, tr.est.}}$: UPRE grid search by $\text{Trace}(A_{\text{TV}})$ estimation; $\text{UPRE}_{\text{golden, tr.est.}}$: UPRE golden Search by $\text{Trace}(A_{\text{TV}})$ estimation.

4.3 Gaussian Additive Noise Variance Estimation Performance

A contrast between the ground truth σ_η^2 for the Gaussian Additive noise corrupted pixels, i.e. the elements which belong to $\mathcal{G}$, and the local variance estimator introduced in Section 3 is elaborated in order to analyze its accuracy. The ground truth variance is defined as $\sigma_{\eta,sample}^2 = \frac{1}{|\mathcal{G}|}\sum_{\mathcal{G}} u(i) - \mu(u)$, where $\mu(u)$ is the sample mean. The test is performed on (gray) Lena, with Gaussian Additive noise with $\sigma_\eta^2 = [\frac{25}{255} - \frac{75}{255}]$ (steps of $\frac{10}{255}$), and Salt and Pepper noise with $s = [0.25 - 0.75]$ (steps of 0.25). Figure 4.2 shows the test results. It is important to remark that the Additive noise is applied to the entire image, so after the Impulse noise corruption, the Additive noise corrupted element set $\mathcal{G}$ not necessarily holds the original σ_η^2. The results show that $\hat{\sigma}_\eta^2$ gets significantly close σ_η^2 in most cases.

4.4 Impulse Noise Outliers Detection Performance

The SAIRN proposed method makes use of the RAMF for outliers detection, which are considered noise corrupted elements under the Salt and Pepper noise scenario. In contrast, the present framework requires an accurate Impulse noise estimation whether on a Mixed noise scenario or in a plain Impulse noise scenario. For this purpose, several Impulse noise estimation methods are evaluated. The methods are: RAMF, PSM, IWF, DWMF, FIDRM Detector, MAD, and a Modification of the CWMF proposed in [4]. This methods, all of them based on two-stage ranked order filters and introduced in Section 2, are tested on a Salt and Pepper over Gaussian Additive noise scenario for a test image set formed by grayscale (Peppers, Cameraman) and color (Goldhill, Lena) images. Figure 4.3 show the image set. For the evaluation, σ_η varies within $[\frac{5}{255} - \frac{15}{255}]$ (steps of $\frac{5}{255}$) and s within $[30\% - 90\%]$ (steps of 0.3). Each test consists of fifteen iterations. Each performance is measured by the ratio of True positives vs. the ground truth noise set, False positives vs. the number of pixels in the image, and the required time for each method. Figures (4.14 - 4.21) show the performance results.

The evaluation shows no method which outperforms the rest. Some methods perform better than others in some scenarios. RAMF attains an impressive True positives ratio for high level Salt and Pepper noise in all the covered Gaussian Noise levels. However, this feature is considerably reduced for low level Salt and Pepper noise. Moreover, in the Cam-

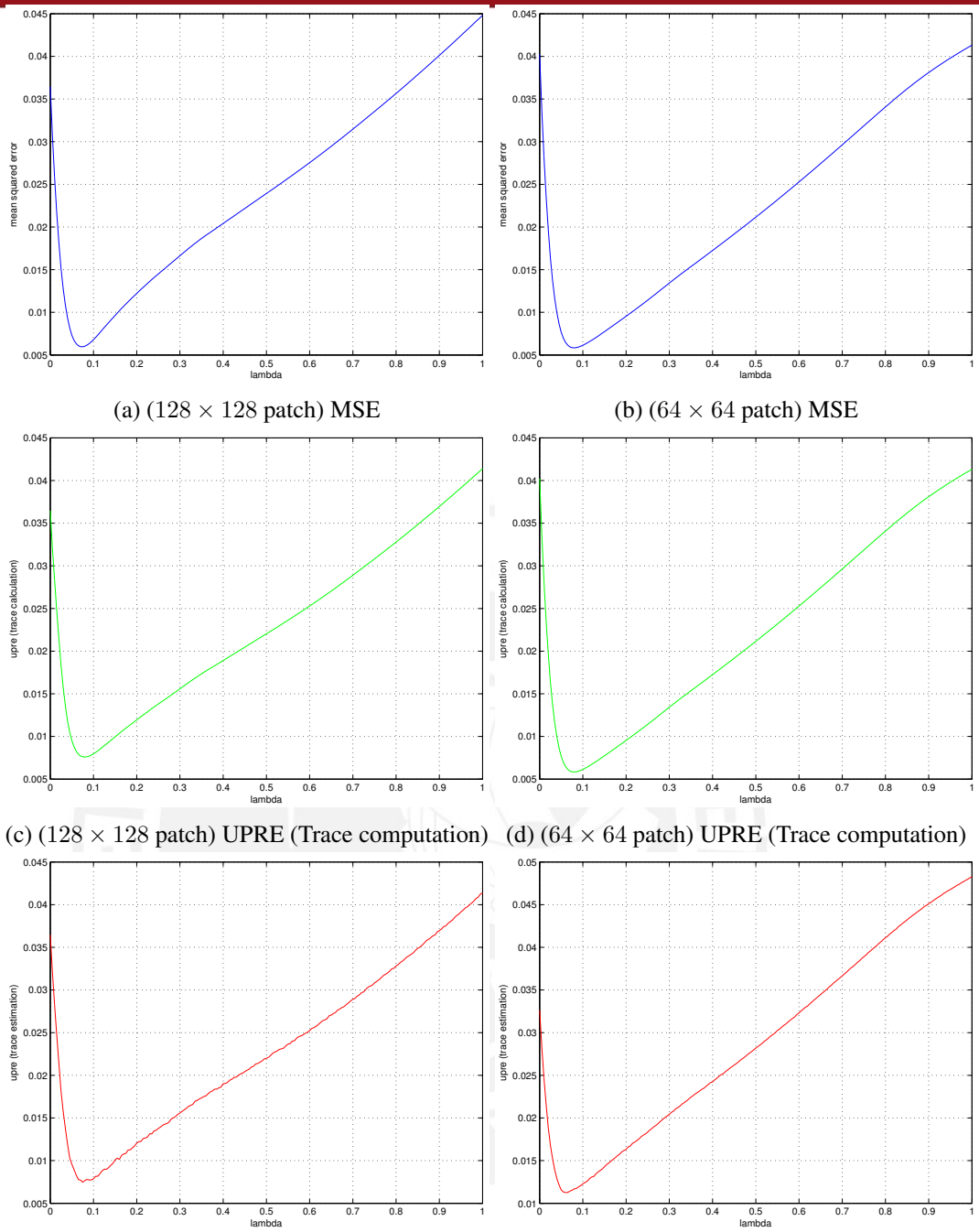

(a) (128 × 128 patch) MSE

(b) (64 × 64 patch) MSE

(c) (128 × 128 patch) UPRE (Trace computation)

(d) (64 × 64 patch) UPRE (Trace computation)

(e) (128 × 128 patch) UPRE (Trace estimation)

(f) (64 × 64 patch) UPRE (Trace estimation)

Figure 4.1: Local risk calculation vs. local risk estimation for (gray) Lena under a grid search.

eraman test, RAMF results show a high False positives ratio on all the covered Gaussian Noise corruption levels. For low level Salt and Pepper noise, the two better results are obtained by RAMF and DWMF. For high level Salt and Pepper noise, the two better results are obtained by RAMF and ACWMF. This pattern is kept in almost all the tests. Regarding the computational requirements, PSM reports at least three times the cost of the rest of methods. Besides this, RAMF reports a required time in the scale of 20 seconds, which is a considerable difference with the rest of methods, which are below 10 seconds.

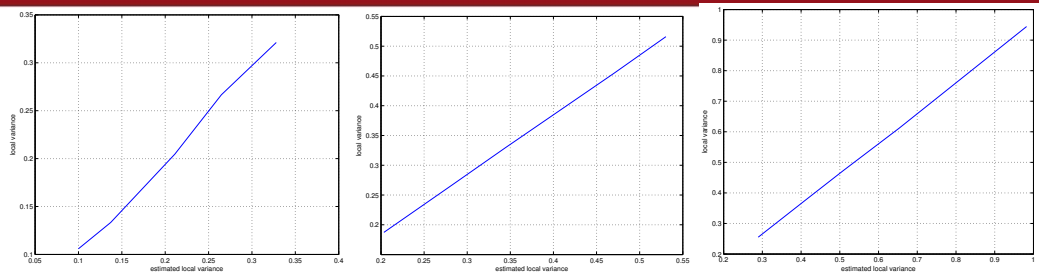

(a) 25% Impulse noise level (b) 50% Impulse noise level (c) 75% Impulse noise level

Figure 4.2: Local variance estimation accuracy.

(a) (gray) Peppers (b) (gray) Cameraman (c) (color) Lena (d) (color) Goldhill

Figure 4.3: Test image set for the Impulse noise estimators evaluation.

Based on this results, it is proposed to combine the output of two Impulse noise detectors in order to get a more accurate noise estimation whether on a Mixed noise scenario or in a plain Salt and Pepper noise scenario. This approach consists on the combination of the RAMF and the DWMF outputs (denoted as $\mathcal{N}_{\text{RAMF}} \cap \mathcal{N}_{\text{DWMF}}$). This filters are chosen based on the fact that DWMF has a great response for low level Impulse noise inputs, while the RAMF has a good response for high level Impulse noise inputs. This aims to hold the features of both, and thus obtain a high True positives ratio and low false positives ratio for any Impulse noise level and Gaussian Additive noise level.

This novel estimation method is put into test and compared to the RAMF, which is used in the SAIRN algorithm. Both ranked order filters are tested on a Mixed noise scenario for a (256 x 256) patch from (gray) Lena. σ_η^2 varies within $[\frac{10}{255} - \frac{50}{255}]$ (steps of $\frac{10}{255}$) and s within $0\% - 90\%$ (steps of 0.15). The performance is measured by the true positives and false positives vs. the ground truth noise set each method achieve. Table 4.3 and 4.4 shows the test results. Figure 4.4 shows the false positives for $\sigma_\eta^2 = \frac{10}{255}$ and s = 0.3. The evaluation shows that the novel approach sustantially decreases the amount of false positives for different s values. Moreover, the true positives almost remain the same in both outputs, which is a favorable feature.

4.5 Impulse Noise Scenario: Image Restoration Performance

The proposed algorithm is contrasted with the results reported for Algorithm III proposed in [2], which is refered as *CHN*, and with the (standard) IRN algorithm [21, 32]. The test images consists of (gray) Bridge, (gray and color) Lena, and (color) Goldhill. Images

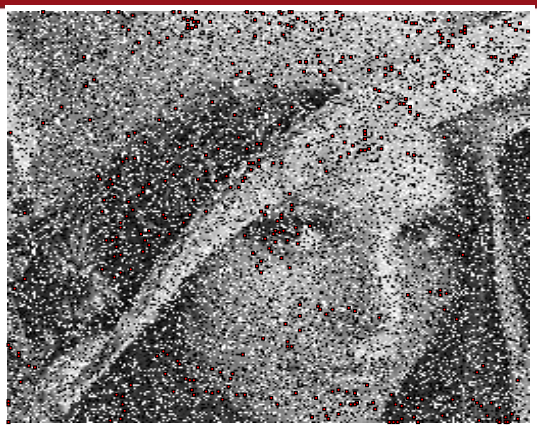

(a) $\mathcal{N}_{\text{RAMF}} \cap \mathcal{N}_{\text{DWMF}}$

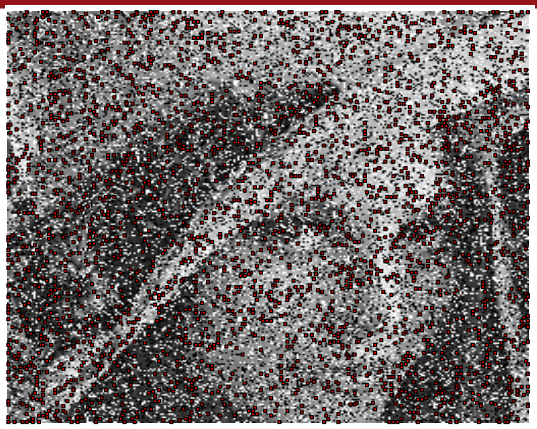

(b) $\mathcal{N}_{\text{RAMF}}$

Figure 4.4: False positives for (gray) Lena (128×128 px.). $s = 0.3, \sigma_\eta^2 = \frac{10}{255}$.

s (elements)	$\sigma_\eta^2 = \frac{10}{255}$		$\sigma_\eta^2 = \frac{20}{255}$		$\sigma_\eta^2 = \frac{30}{255}$		$\sigma_\eta^2 = \frac{40}{255}$		$\sigma_\eta^2 = \frac{50}{255}$	
	$\mathcal{R} \cap \mathcal{D}$	$\mathcal{R}$	$\mathcal{R} \cap \mathcal{D}$	$\mathcal{R}$	$\mathcal{R} \cap \mathcal{D}$	$\mathcal{R}$	$\mathcal{R} \cap \mathcal{D}$	$\mathcal{R}$	$\mathcal{R} \cap \mathcal{D}$	$\mathcal{R}$
0(0)	1269	10920	3101	12512	6279	13222	9063	13769	11207	13928
0.15(10032)	629	5462	1554	6390	3175	6691	4724	6874	5575	6796
0.3(19779)	389	2629	828	2968	1692	3160	2350	3213	2644	3202
0.45(29775)	200	1119	495	1324	743	1221	974	1281	1100	1322
0.6(39399)	85	316	185	380	239	371	296	376	337	402
0.75(49298)	20	60	40	59	47	58	53	65	68	72
0.9(59022)	55	68	59	63	63	68	53	57	88	90

Table 4.3: Impulse noise detectors performance for the Impulse over Gaussian Additive noise scenario: False positives. $\mathcal{R} : \mathcal{N}_{\text{RAMF}}$, $\mathcal{D} : \mathcal{N}_{\text{DWMF}}$.

are shown in Figure 4.5. This test images were corrupted with Impulse noise with $s = [0.1 - 0.9]$ (steps of 0.2), which matches the experimental setup in [2].

(a) (gray) Bridge

(b) (gray) Lena

(c) (color) Lena

(d) (color) Goldhill

Figure 4.5: Impulse noise scenario test image set.

s (elements)	$\hat{\sigma}_\eta^2 = \frac{10}{255}$		$\hat{\sigma}_\eta^2 = \frac{20}{255}$		$\hat{\sigma}_\eta^2 = \frac{30}{255}$		$\hat{\sigma}_\eta^2 = \frac{40}{255}$		$\hat{\sigma}_\eta^2 = \frac{50}{255}$	
	$\mathcal{R} \cap \mathcal{D}$	$\mathcal{R}$	$\mathcal{R} \cap \mathcal{D}$	$\mathcal{R}$	$\mathcal{R} \cap \mathcal{D}$	$\mathcal{R}$	$\mathcal{R} \cap \mathcal{D}$	$\mathcal{R}$	$\mathcal{R} \cap \mathcal{D}$	$\mathcal{R}$
0(0)	0	0	0	0	0	0	0	0	0	0
0.15(10032)	9714	9927	9804	9804	9849	9849	9856	9856	10032	10032
0.3(19779)	19779	19779	19625	2968	19710	3160	19607	3213	19702	3202
0.45(29775)	29843	1119	29937	1324	29775	1221	29489	1281	29708	1322
0.6(39399)	39150	39150	39296	39296	39149	39149	39394	39394	39312	39312
0.75(49298)	49201	49201	49007	49007	49038	49038	48991	48991	49298	49298
0.9(59022)	58399	58936	58499	59022	57657	58825	58125	58955	57547	58973

Table 4.4: Impulse noise detectors performance for the Impulse over Gaussian Additive noise scenario: True positives. $\mathcal{R} : \mathcal{N}_{\text{RAMF}}$; $\mathcal{D} : \mathcal{N}_{\text{DWMF}}$.

Image	Noise	SNR (dB)		PSNR (dB)			SSIM [36]	
		IRN	SA-IRN	IRN	SA-IRN	CHN	IRN	SA-IRN
Lena (gray)	0.5	12.8734	19.9870	26.4388	34.1221	≈34	0.8074	0.9419
	0.7	10.1669	16.4732	23.5971	30.6190	29.3	0.7283	0.8934
	0.9	2.3549	11.5379	14.3488	25.4222	25.4	0.5249	0.7760
Bridge (gray)	0.5	8.5561	13.8882	21.7991	27.1569	≈27	0.4941	0.8611
	0.7	7.0238	11.1691	20.0541	24.4027	25	0.3908	0.7396
	0.9	2.0901	7.6764	13.0018	20.9045	21.5	0.2371	0.4920
Lena (color)	0.5	16.2371	21.8106	28.9538	34.5205	–	–	–
	0.7	12.6595	18.7444	25.3708	31.4553	–	–	–
	0.9	2.8881	14.1123	15.1128	26.7976	–	–	–
Goldhill (color)	0.5	15.2090	20.4090	27.6639	32.9757	–	–	–
	0.7	12.0941	17.3832	24.8784	30.0075	–	–	–
	0.9	2.3510	13.2910	14.7308	25.7874	–	–	–

Table 4.5: Computation of the reconstructed image quality reached by the Spatially Adaptive IRN algorithm, the standard IRN algorithm, and the CHN$^{(1)}$ algorithm.$^{(1)}$ Information taken from [2, Fig. 2 - Fig. 5]. Results shown in dB

Noise level	(gray) Lena		(gray) Bridge		(color) Lena		(color) Goldhill	
	N. detector	Iter. ℓ-1 TV	N. detector	Iter. ℓ-1 TV	N. detector	Iter. ℓ-1 TV	N. detector	Iter. ℓ-1 TV
0.1	0.65	23.35	0.89	32.25	1.99	80.41	3.17	131.40
0.3	1.91	28.30	2.18	35.04	5.87	95.95	9.36	164.29
0.5	3.54	32.93	3.81	35.69	10.95	119.69	17.46	198.26
0.7	6.23	41.61	6.53	42.79	18.92	144.26	29.86	241.40
0.9	14.40	57.74	14.72	56.5	43.88	211.11	69.26	339.96

Table 4.6: Processing time for the Spatially Adaptive IRN algorithm. Results shown in seconds.

For all experiments we use $w_{\max} = 9$ (see section 3.1.3), and $\rho = 0.65$ and $\sigma = 0.5$ (see (3.15)). Also, we use five global iterations with eight local iterations ($M = 5$ and $K = 8$ in Algorithm 2), which seems to be a good compromise between the computational cost and the reconstruction quality.

As expected, both the CHN and the spatially adaptive IRN algorithm outperform the (standard) IRN algorithm. We also note that the CHN and the proposed algorithm have very similar performance for the grayscale case since both use the RAMF as noise estimation method. Table 4.5 shows the reconstruction performance for the IRN, CHN, and the proposed algorithm. This information is based on the average of ten different trials. Figures (4.6 - 4.9) show the noisy test images, and their respective reconstruction images, based on the proposed algorithm.

The execution time for the proposed algorithm is split into two specific tasks: Corrupted-pixel set detection and Iterative Minimization based on the IRN algorithm. Table 4.6 shows that the iterative procedure has a predominant weight in the computational time, although the noise detection step increases with the noise level, which is expected. Moreover, the computational performance of the spatially adaptive IRN outperforms that of the CHN algorithm ([2, Table II]) by a factor of 100 to 1 for images with 70% and 90% of noise corruption. Considering a correction factor for the CPUs available seven years ago ([2] was published in 2005), this is still a significant computational improvement.

(a) 70% noisy (b) 90% noisy (c) Rec. 70% (PSNR: 24.4 dB) (d) Rec. 90% (PSNR: 20.90 dB)

Figure 4.6: Impulse noise image denoising for (gray) Bridge.

(a) 70% noisy (b) 90% noisy (c) Rec. 70% (PSNR: 30.61 dB) (d) Rec. 90% (PSNR: 25.42 dB)

Figure 4.7: Impulse noise image denoising for (gray) Lena.

(a) 70% noisy (b) 90% noisy (c) Rec. 70% (PSNR: 31.45 dB) (d) Rec. 90% (PSNR: 26.79 dB)

Figure 4.8: Impulse noise image denoising for (color) Lena.

(a) 70% noisy (b) 90% noisy (c) Rec. 70% (PSNR: 30 dB) (d) Rec. 90% (PSNR: 25.78 dB)

Figure 4.9: Impulse noise image denoising for (color) Goldhill.

4.6 Impulse over Gaussian Additive Noise Scenario: Image Restoration Performance

The framework composed by the previously evaluated algorithms is analyzed as a global system under the worst case scenario of interest: Impulse over Gaussian Additive noise. In order to test its performance, a grayscale image set based on four different images is corrupted by Gaussian Additive noise with $\sigma_\eta^2 : [\frac{5}{255}, \frac{15}{255}]$ (steps of $\frac{5}{255}$), and Salt and

Image	s ($\sigma_\eta^2 = \frac{5}{255}$)	SNR		PSNR				SSIM	
		ROD	**Proposed**	XIA	CAI	ROD	**Proposed**	ROD	**Proposed**
Lena (gray)	0.3	20.11	16.17	36.20	34.15	34.64	34.23	0.89	0.9091
	0.5	18.21	14.1	33.93	32.30	32.75	31.99	0.87	0.8854
	0.7	15.66	12.62	30.76	29.73	30.20	29.74	0.83	0.8418
Cameraman (gray)	0.3	–	15.18	31.92	29.90	–	36.06	–	0.9323
	0.5	–	13.83	29	27.40	–	33.38	–	0.9187
	0.7	–	11.98	25.51	24.67	–	29.7	–	0.8857
Peppers (gray)	0.3	–	14.1389	35.50	33.87	–	33.0612	–	0.8862
	0.5	–	12.7962	33.38	31.83	–	30.2727	–	0.8539
	0.7	–	11.7403	30.81	29.58	–	28.2741	–	0.8272

Table 4.7: Reconstruction quality comparison for the CAI[(1)], XIA[(1)], ROD[(2)] and the proposed algorithm. $\sigma_\eta^2 = \frac{5}{255}$. [(1)] Information taken from [3]. [(2)] Information taken from [4]. Results shown in dB

Pepper noise with $s : [0.1, 0.7]$ (steps of 0.1). Figure 4.10 show the test image set.

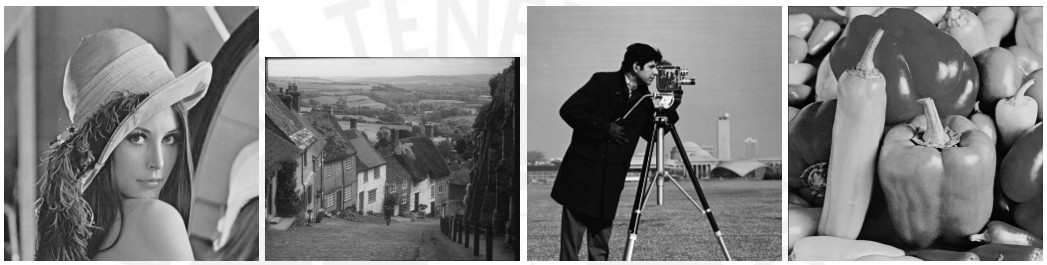

(a) (gray) Lena (b) (gray) Goldhill (c) (gray) Cameraman (d) (gray) Peppers

Figure 4.10: Impulse over Gaussian Additive noise test image set.

Quality results are measured and compared with the documented results from [35], [3] and [4] (denominated (CAI), (XIA) and (ROD) respectively). Furthermore, the processing time is also taken into account in the performance evaluation. Tables (4.7, 4.8, 4.9) show the full results and algorithms contrast, respectively. Figures (4.22 - 4.24) shows the reconstruction stages for the $(\sigma_\eta^2, s) = [(\frac{5}{255}, 0.3), (\frac{10}{255}, 0.5), (\frac{15}{255}, 0.7)]$ case for the test image set. Regarding the experimental setup, the following parameter values were used:

- UPRE$_{\text{TV}}$: $\beta = 10^{-5}$, Trace Estimation Iterations$_{max} = 15$, Search Ratio$= \frac{1+\sqrt{5}}{2}$, Search Range$= [0, 1]$, Search Iterations$_{max} = 10$.
- IRN(ℓ_{TV}^2): Loops$_{inner} = 20$, Solver Tolerance$= 10^{-4}$, $\epsilon_F = 10^{-2}$, $\epsilon_R = 10^{-4}$.
- SAIRN(ℓ_{TV}^1) λ Update Scheme: fixed at 10, Loops$_{inner} = 20$, Loops$_{outer} = 10$, Solver Tolerance$= 10^{-4}$, $\epsilon_F = 10^{-2}$, $\epsilon_R = 10^{-4}$.
- RAMF: W$= 5 \times 5$.
- DWMF: W$= 5 \times 5$, $T_d = \frac{510}{255}$ (normalized intensities).

From the results, the obvious disadvantage the proposed algorithm introduces is the overdemanding time it requires, which is more than two orders bigger than the rest of studied methods. Even for a UPRE estimation based on a search criteria (not a grid search), and a relaxation in the error tolerance, the required time is extremely high. This stage is the one

Image	s ($\sigma_\eta^2 = \frac{5}{255}$)	SNR		PSNR				SSIM	
		ROD	**Proposed**	XIA	CAI	ROD	**Proposed**	ROD	**Proposed**
Lena (gray)	0.3	17.82	14.0159	33.19	31.33	32.36	31.8893	0.83	0.8581
	0.5	16.61	13.2528	31.51	29.88	31.14	30.1793	0.81	0.8358
	0.7	14.54	12.1933	28.98	28.11	29.07	28.0757	0.78	0.8035
Cameraman (gray)	0.3	–	13.8010	29.79	27.71	–	31.8893	–	0.9118
	0.5	–	12.9715	27.71	25.99	–	30.1793	–	0.8563
	0.7	–	11.5333	24.16	23.45	–	28.0757	–	0.8348
Peppers (gray)	0.3	–	13.3477	33.23	31.66	–	31.4600	–	0.8427
	0.5	–	12.4770	31.82	30.24	–	29.7761	–	0.8173
	0.7	–	11.3633	29.39	28.43	–	27.6307	–	0.7832

Table 4.8: Reconstruction quality comparison for the CAI$^{(1)}$, XIA$^{(1)}$, ROD$^{(2)}$ and the proposed algorithm. $\sigma_\eta^2 = \frac{10}{255}$. $^{(1)}$ Information taken from [3]. $^{(2)}$ Information taken from [4]. Results shown in dB

Image	s ($\sigma_\eta^2 = \frac{15}{255}$)	SNR		PSNR				SSIM	
		ROD	**Proposed**	XIA	CAI	ROD	**Proposed**	ROD	**Proposed**
Lena (gray)	0.3	16.03	12.2192	31.49	29.67	30.56	30.3238	0.76	0.8307
	0.5	15.27	11.6562	29.95	28.42	29.80	29.0079	0.75	0.7894
	0.7	13.80	10.7833	27.53	26.48	28.33	27.4080	0.74	0.7635
Cameraman (gray)	0.3	–	12.8200	28.25	26.10	–	31.0199	–	0.8821
	0.5	–	12.2386	26.19	24.69	–	29.9021	–	0.8250
	0.7	–	11.0884	23.13	22.67	–	28.0336	–	0.7552
Peppers (gray)	0.3	–	12.6931	31.75	30.25	–	30.1528	–	0.8139
	0.5	–	12.0372	30.37	28.85	–	28.8289	–	0.7877
	0.7	–	11.0469	27.89	27.07	–	27.3034	–	0.7534

Table 4.9: Reconstruction quality comparison for the CAI$^{(1)}$, XIA$^{(1)}$, ROD$^{(2)}$ and the proposed algorithm. $\sigma_\eta^2 = \frac{15}{255}$. $^{(1)}$ Information taken from [3]. $^{(2)}$ Information taken from [4]. Results shown in dB

Algorithm	s	$\sigma_\eta^2 = \frac{5}{255}$	$\sigma_\eta^2 = \frac{15}{255}$
XIA	0.3	93	143
	0.5	119	248
CAI	0.3	338	215
	0.5	247	176
ROD	0.3	34.5	32.8
	0.5	26.9	41.8
Proposed	0.3	1610.9	1654.3
	0.5	1622	1663.2

Table 4.10: Processing Time for the XIA$^{(1)}$, CAI$^{(1)}$, ROD$^{(2)}$ and the proposed algorithm. $^{(1)}$ Information taken from [3]. $^{(2)}$ Information taken from [4]. Results shown in s.

which introduces the most amount of processing time due to the fact that each estimation step requires to find the TV solution for the actual λ. Moreover, since the test images are of a considerable size (512×512), constantly finding TV solutions is an expensive task.

Besides this, the algorithm achieves a reconstruction quality slightly below the other studied methods for the SNR and PSNR metrics. However, based on the SSIM results, the reconstruction structure for the proposed algorithm is more coherent to the original structure than the rest of methods.

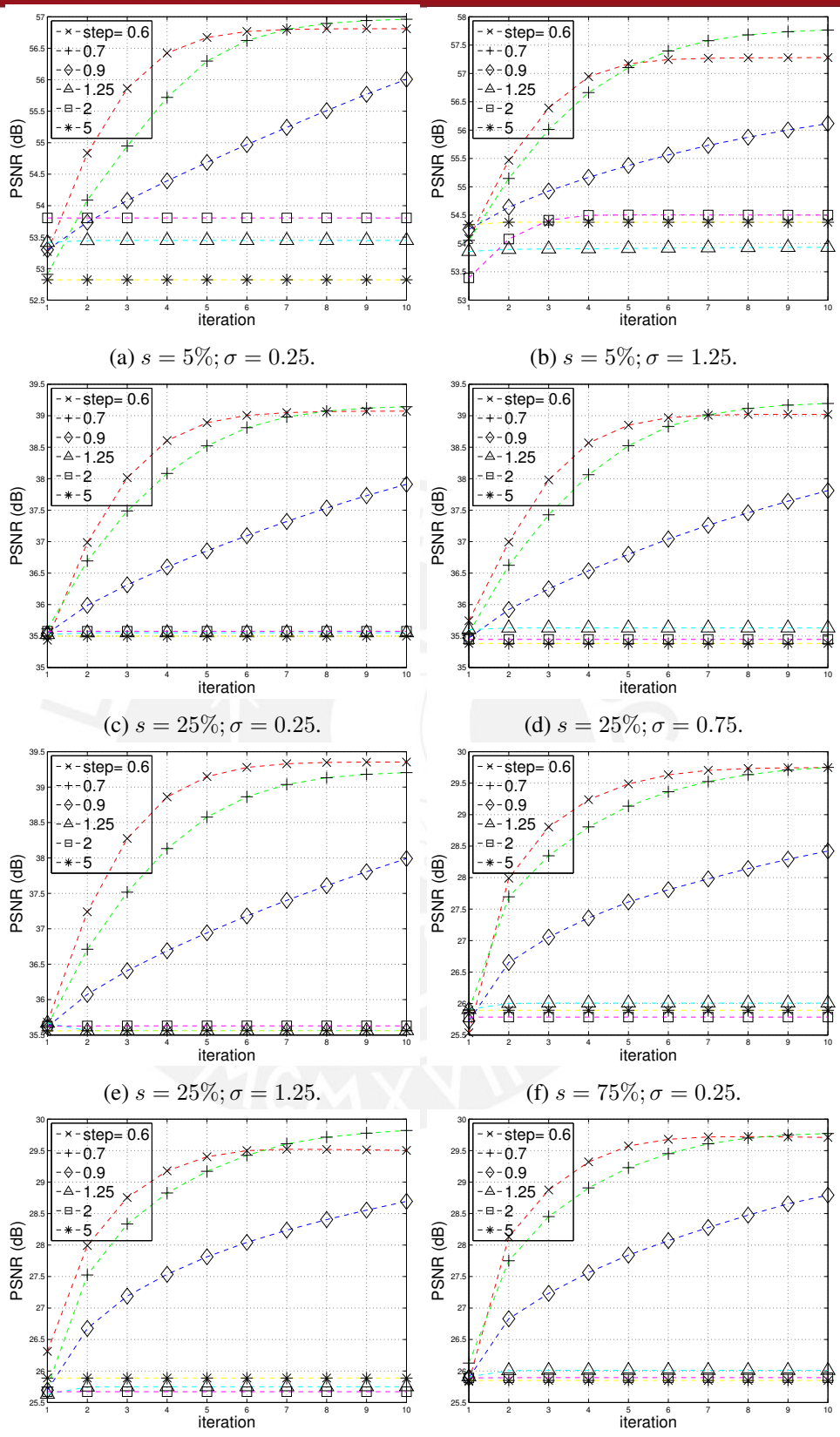

(a) $s = 5\%; \sigma = 0.25$.

(b) $s = 5\%; \sigma = 1.25$.

(c) $s = 25\%; \sigma = 0.25$.

(d) $s = 25\%; \sigma = 0.75$.

(e) $s = 25\%; \sigma = 1.25$.

(f) $s = 75\%; \sigma = 0.25$.

(g) $s = 75\%; \sigma = 0.75$.

(h) $s = 75\%; \sigma = 1.25$.

Figure 4.11: SAIRN update parameters quality impact for (gray) Lena.

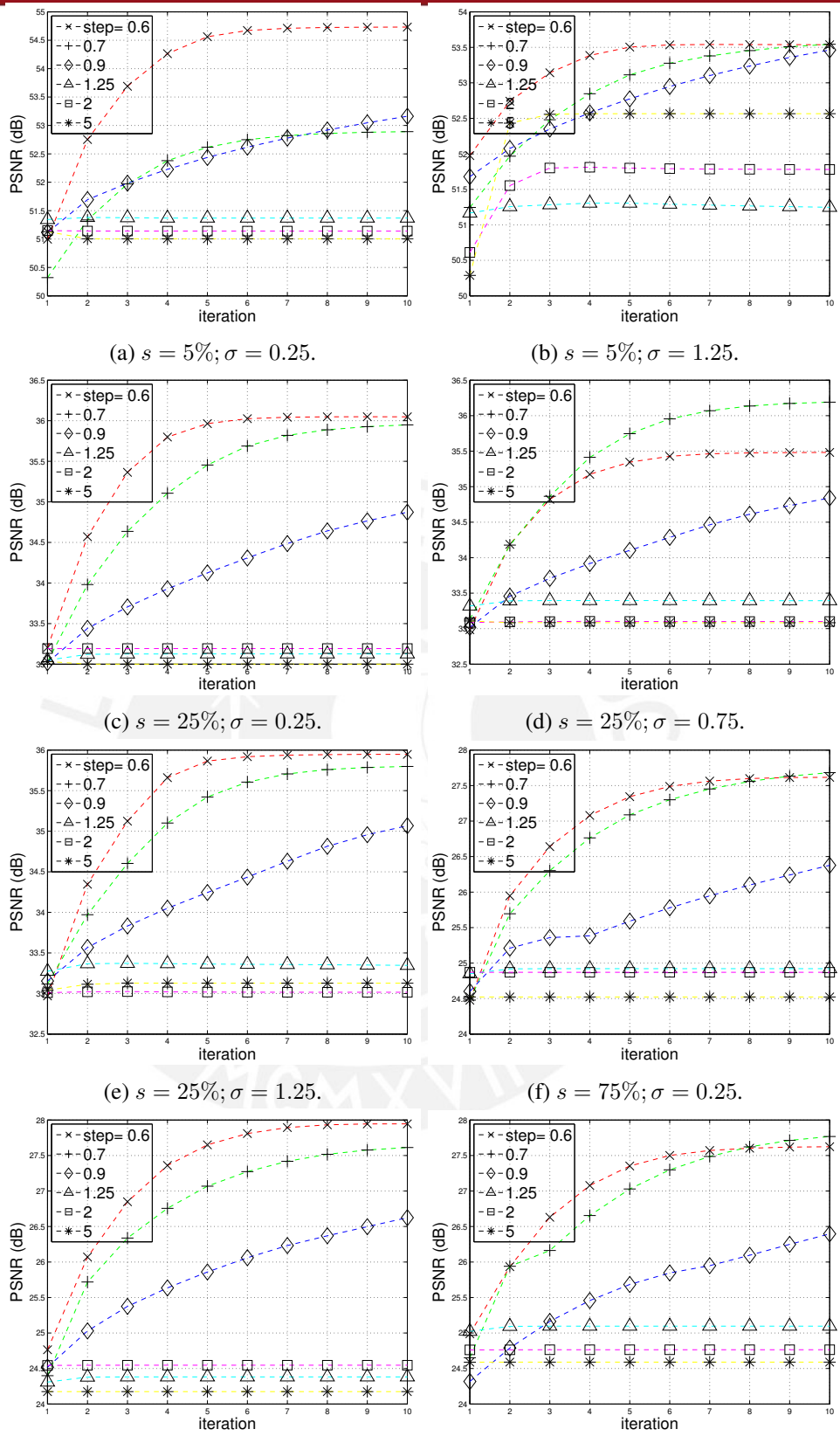

(a) $s = 5\%; \sigma = 0.25$. (b) $s = 5\%; \sigma = 1.25$.

(c) $s = 25\%; \sigma = 0.25$. (d) $s = 25\%; \sigma = 0.75$.

(e) $s = 25\%; \sigma = 1.25$. (f) $s = 75\%; \sigma = 0.25$.

(g) $s = 75\%; \sigma = 0.75$. (h) $s = 75\%; \sigma = 1.25$.

Figure 4.12: SAIRN update parameters quality impact for (gray) Peppers.

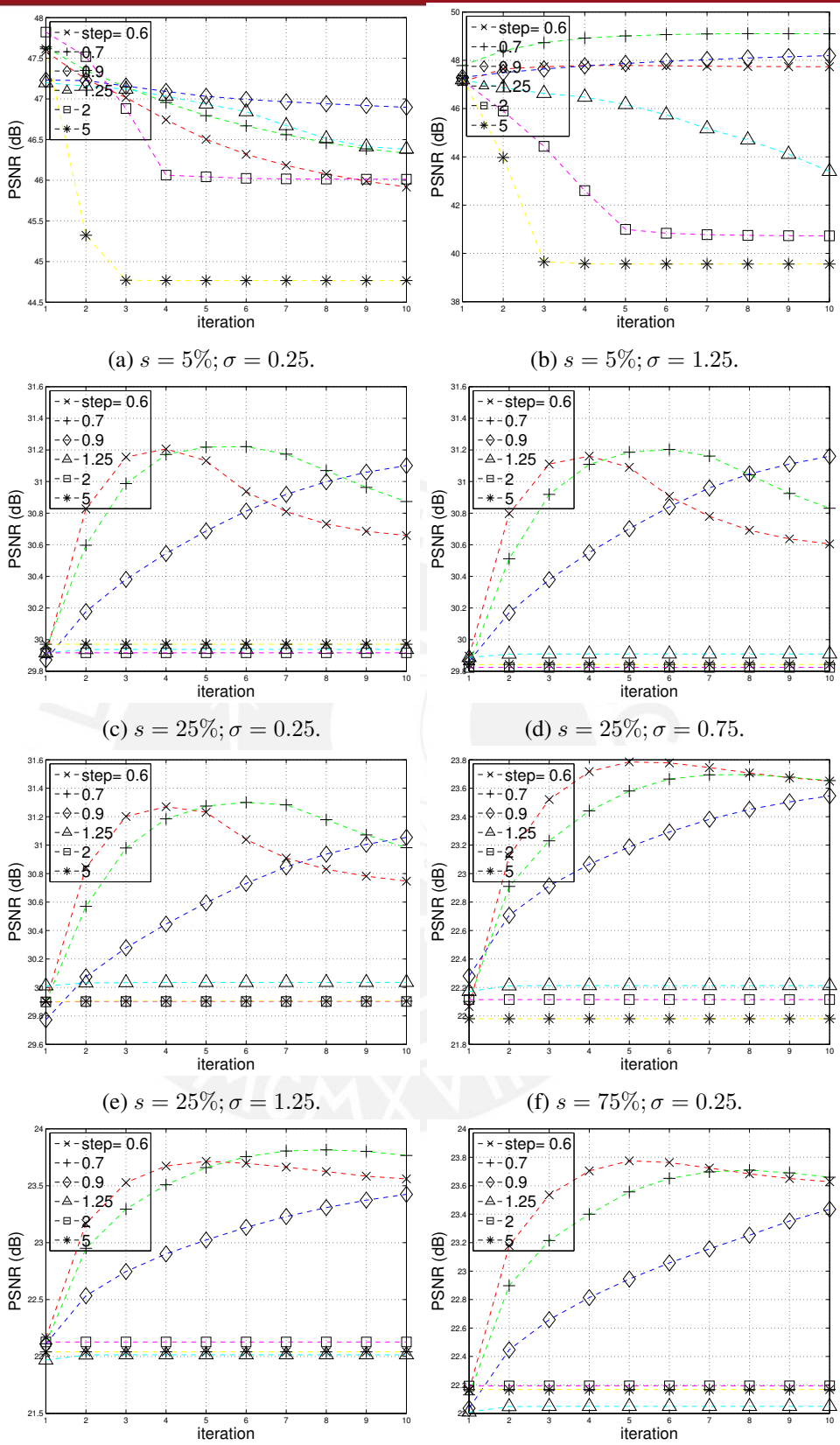

(a) $s = 5\%; \sigma = 0.25$. (b) $s = 5\%; \sigma = 1.25$.

(c) $s = 25\%; \sigma = 0.25$. (d) $s = 25\%; \sigma = 0.75$.

(e) $s = 25\%; \sigma = 1.25$. (f) $s = 75\%; \sigma = 0.25$.

(g) $s = 75\%; \sigma = 0.75$. (h) $s = 75\%; \sigma = 1.25$.

Figure 4.13: SAIRN update parameters quality impact for (gray) Bridge.

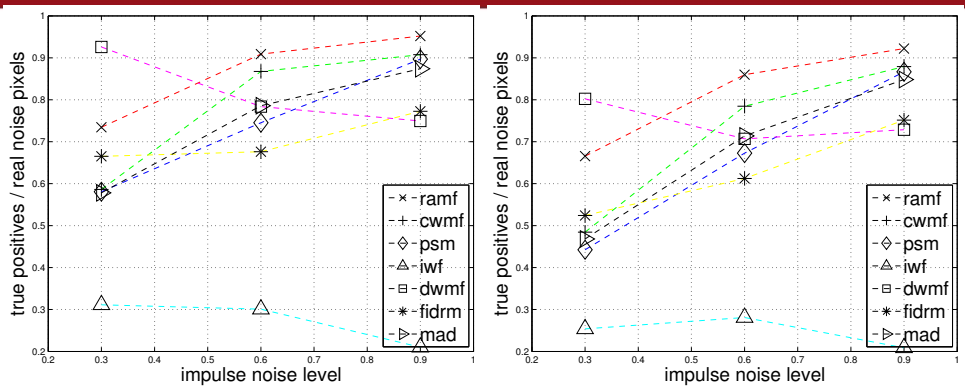

(a) True positives ($\sigma_\eta^2 = \frac{5}{255}$)

(b) True positives ($\sigma_\eta^2 = \frac{10}{255}$)

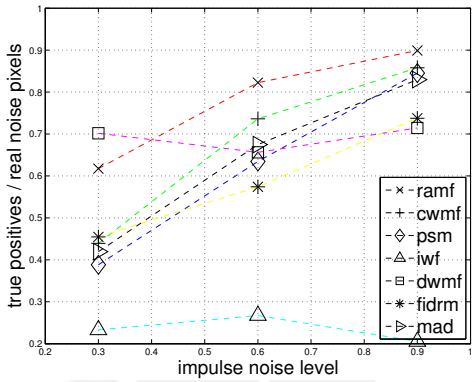

(c) True positives ($\sigma_\eta^2 = \frac{15}{255}$)

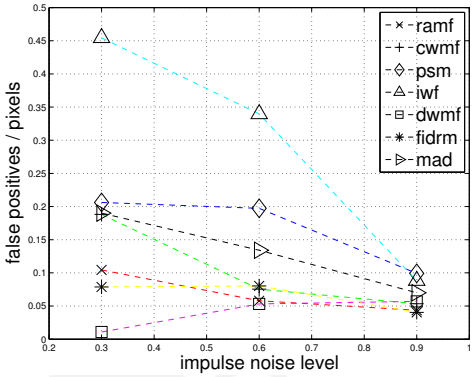

(d) False positives ($\sigma_\eta^2 = \frac{5}{255}$)

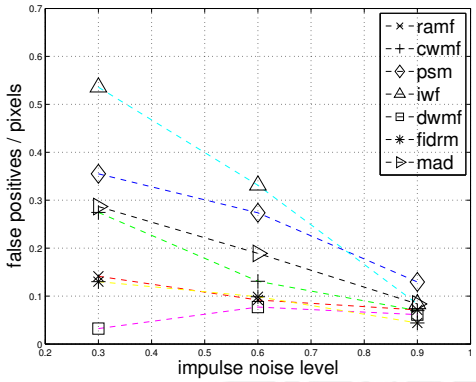

(e) False positives ($\sigma_\eta^2 = \frac{10}{255}$)

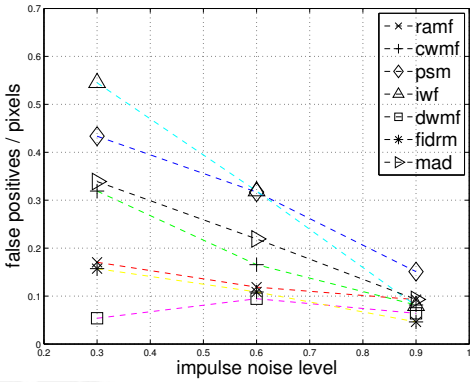

(f) False positives ($\sigma_\eta^2 = \frac{15}{255}$)

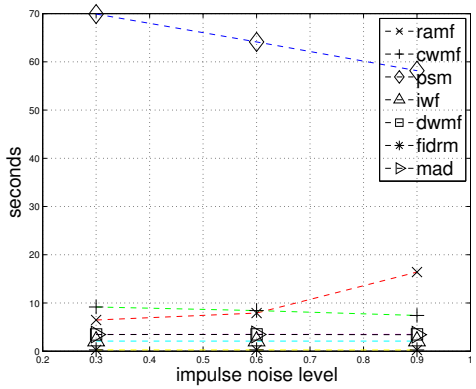

(g) Processing time ($\sigma_\eta^2 = \frac{5}{255}$)

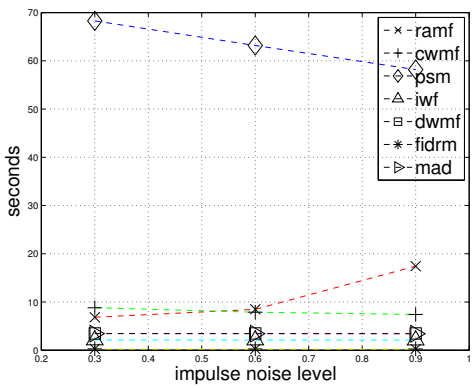

(h) Processing time ($\sigma_\eta^2 = \frac{15}{255}$)

Figure 4.14: Impulse noise detection performance for the Impulse over Gaussian Additive noise scenario for (gray) Peppers.

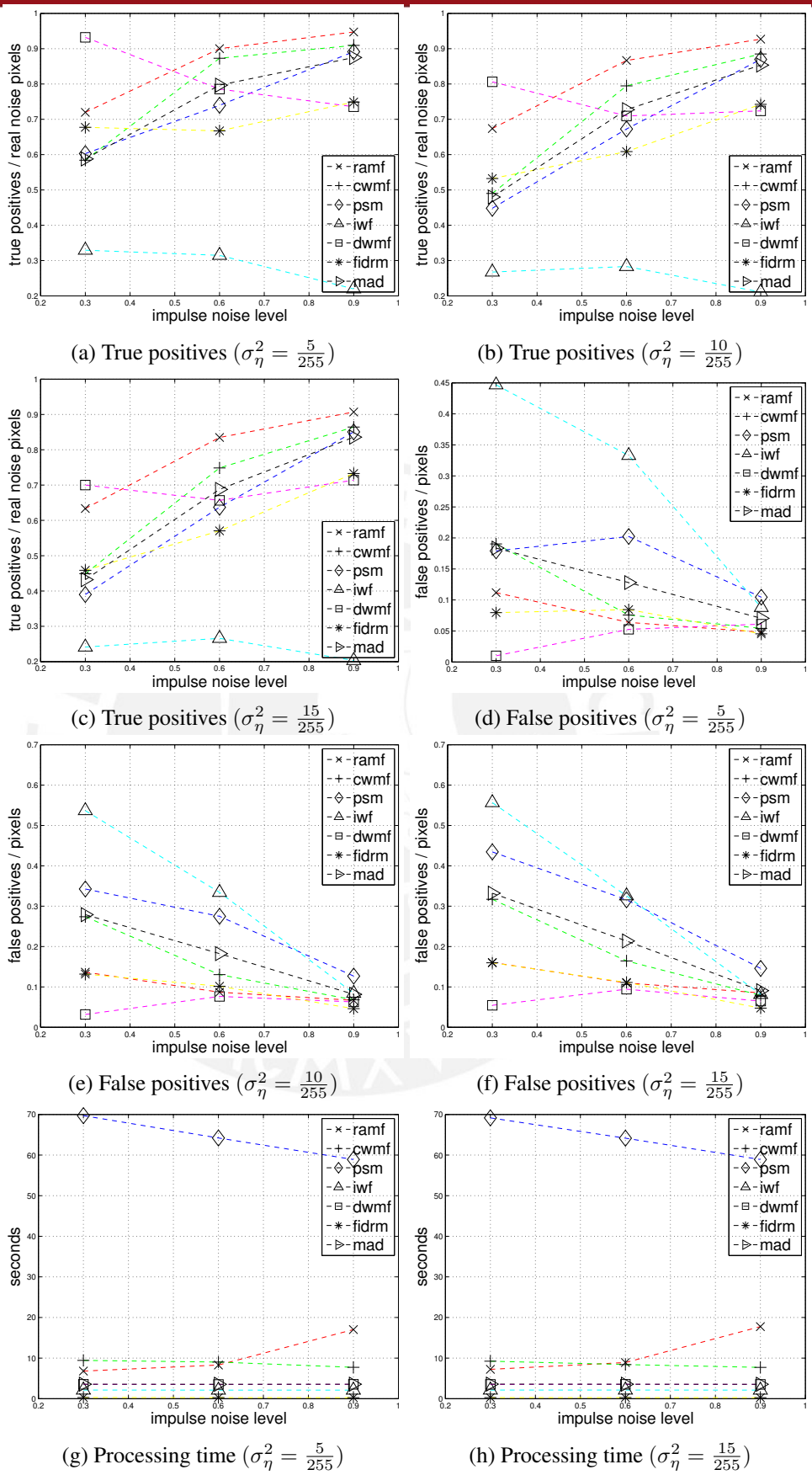

(a) True positives ($\sigma_\eta^2 = \frac{5}{255}$)

(b) True positives ($\sigma_\eta^2 = \frac{10}{255}$)

(c) True positives ($\sigma_\eta^2 = \frac{15}{255}$)

(d) False positives ($\sigma_\eta^2 = \frac{5}{255}$)

(e) False positives ($\sigma_\eta^2 = \frac{10}{255}$)

(f) False positives ($\sigma_\eta^2 = \frac{15}{255}$)

(g) Processing time ($\sigma_\eta^2 = \frac{5}{255}$)

(h) Processing time ($\sigma_\eta^2 = \frac{15}{255}$)

Figure 4.15: Impulse noise detection performance for the Impulse over Gaussian Additive noise scenario for (gray) Cameraman.

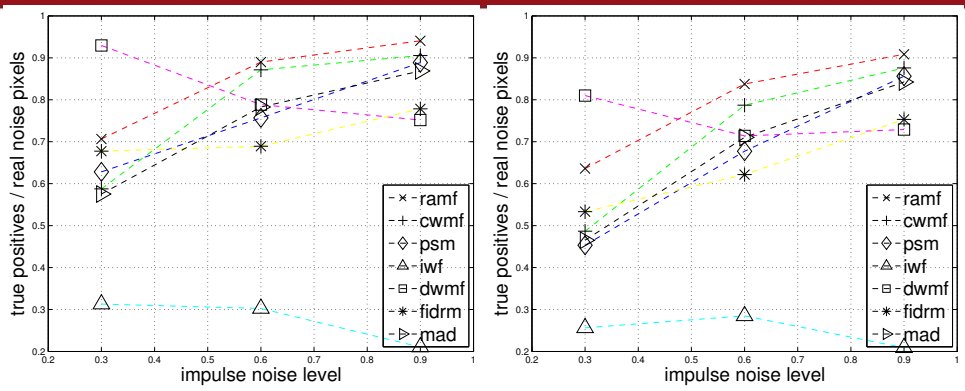

(a) True positives ($\sigma_\eta^2 = \frac{5}{255}$)

(b) True positives ($\sigma_\eta^2 = \frac{10}{255}$)

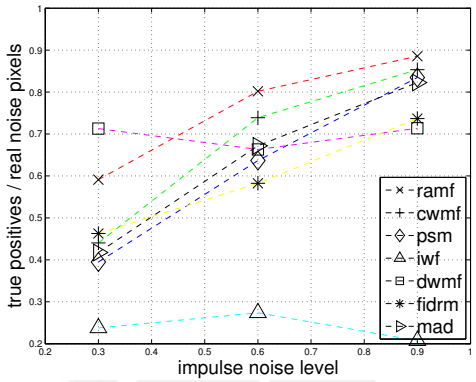

(c) True positives ($\sigma_\eta^2 = \frac{15}{255}$)

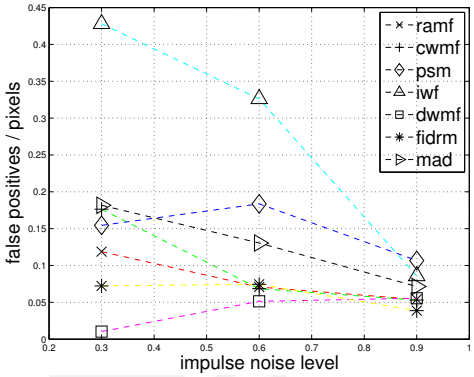

(d) False positives $\sigma_\eta^2 = \frac{5}{255}$

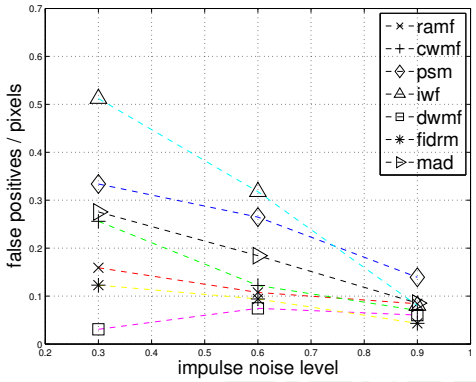

(e) False positives $\sigma_\eta^2 = \frac{10}{255}$

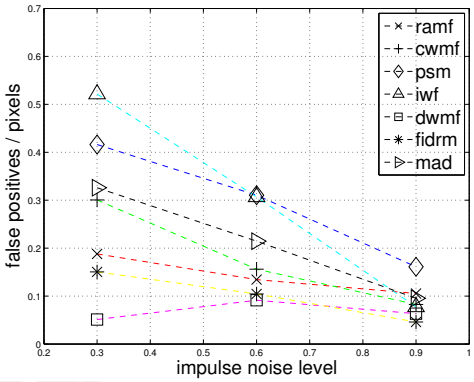

(f) False positives $\sigma_\eta^2 = \frac{5}{255}$

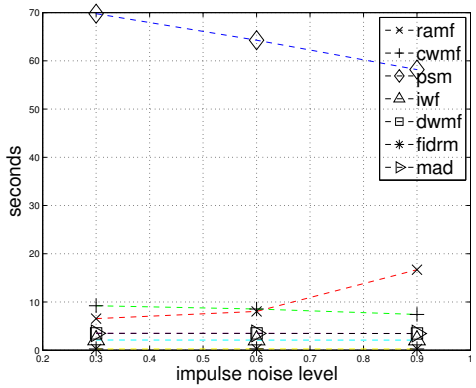

(g) Processing time $\sigma_\eta^2 = \frac{15}{255}$

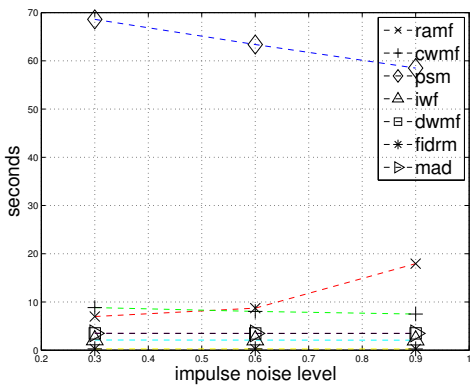

(h) Processing time $\sigma_\eta^2 = \frac{5}{255}$

Figure 4.16: Impulse noise detection performance for the Impulse over Gaussian Additive noise scenario for (color layer 1) Lena.

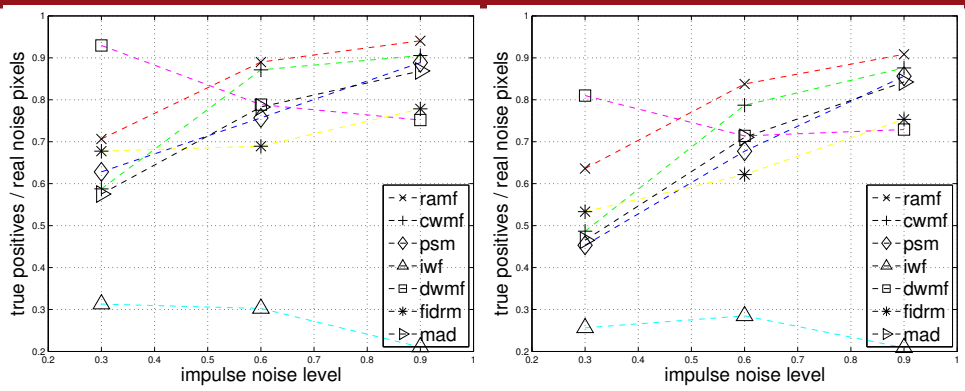

(a) True positives $\sigma_\eta^2 = \frac{10}{255}$

(b) True positives $\sigma_\eta^2 = \frac{15}{255}$

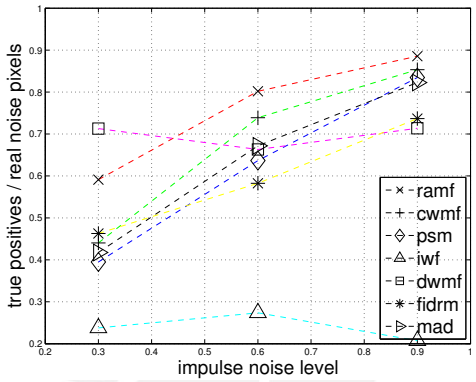

(c) True positives $\sigma_\eta^2 = \frac{5}{255}$

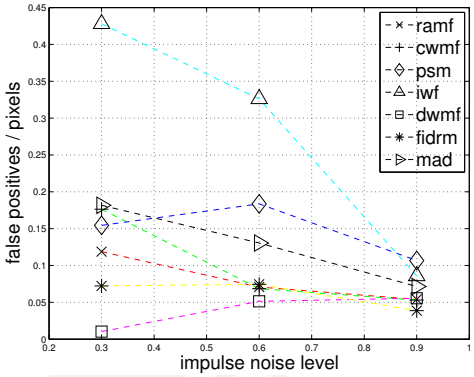

(d) False positives $\sigma_\eta^2 = \frac{10}{255}$

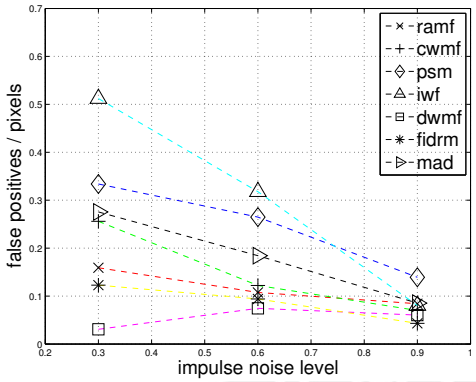

(e) False positives $\sigma_\eta^2 = \frac{15}{255}$

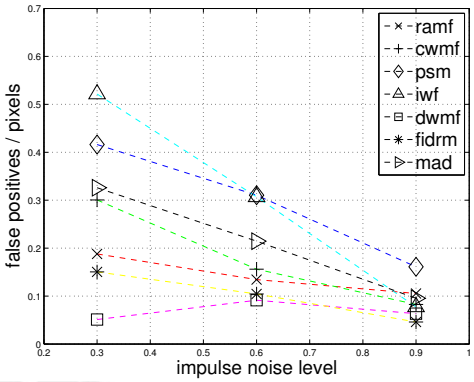

(f) False positives $\sigma_\eta^2 = \frac{5}{255}$

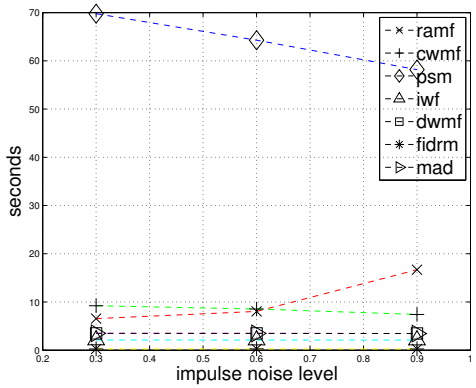

(g) Processing time $\sigma_\eta^2 = \frac{15}{255}$

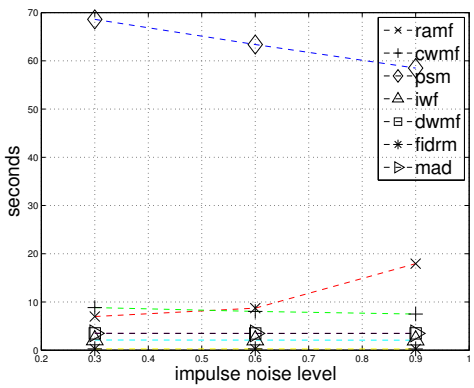

(h) Processing time $(\sigma_\eta^2 = \frac{5}{255})$

Figure 4.17: Impulse noise detection performance for the Impulse over Gaussian Additive noise scenario for (color layer 2) Lena.

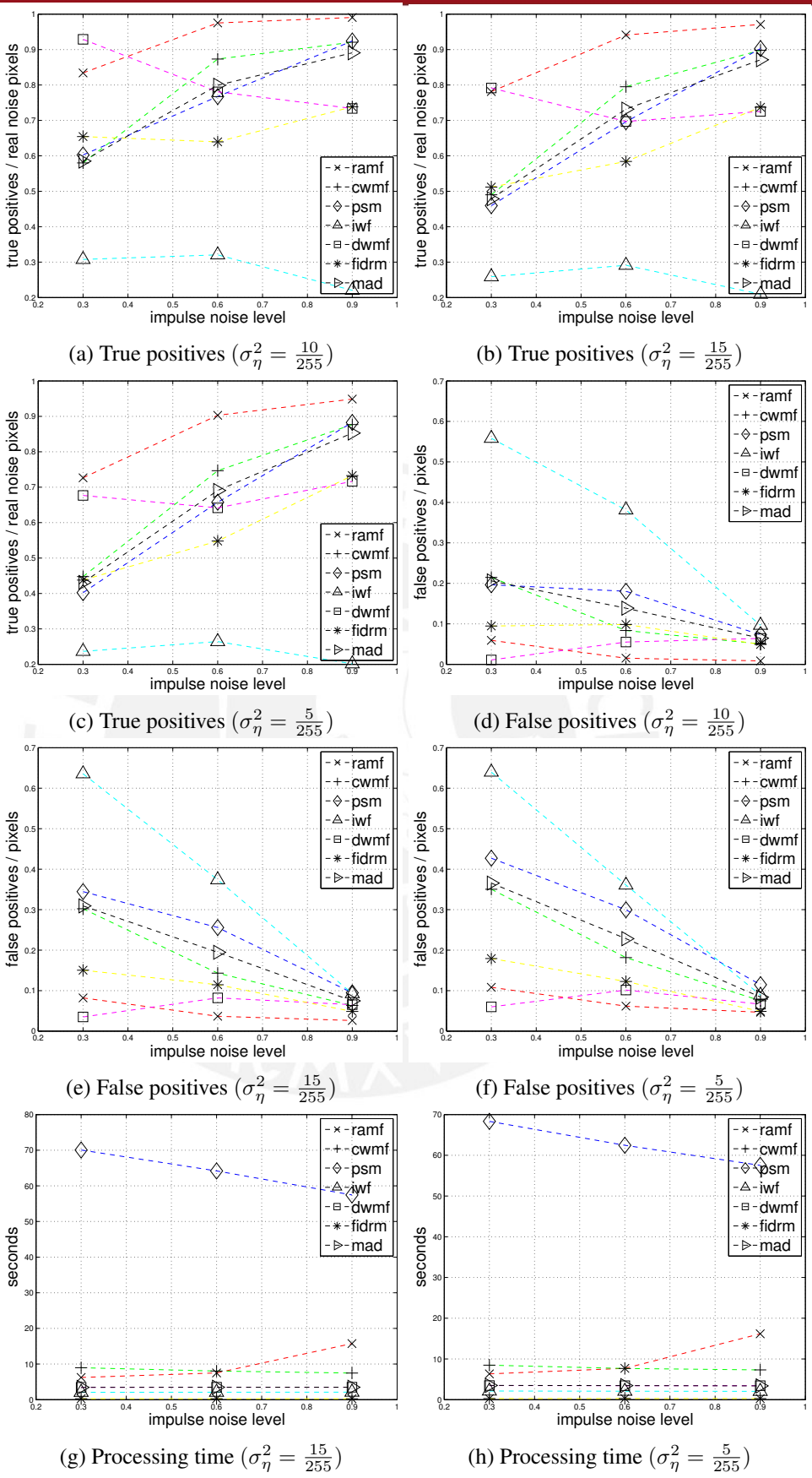

(a) True positives ($\sigma_\eta^2 = \frac{10}{255}$)

(b) True positives ($\sigma_\eta^2 = \frac{15}{255}$)

(c) True positives ($\sigma_\eta^2 = \frac{5}{255}$)

(d) False positives ($\sigma_\eta^2 = \frac{10}{255}$)

(e) False positives ($\sigma_\eta^2 = \frac{15}{255}$)

(f) False positives ($\sigma_\eta^2 = \frac{5}{255}$)

(g) Processing time ($\sigma_\eta^2 = \frac{15}{255}$)

(h) Processing time ($\sigma_\eta^2 = \frac{5}{255}$)

Figure 4.18: Impulse noise detection performance for the Impulse over Gaussian Additive noise scenario for (color layer 3) Lena.

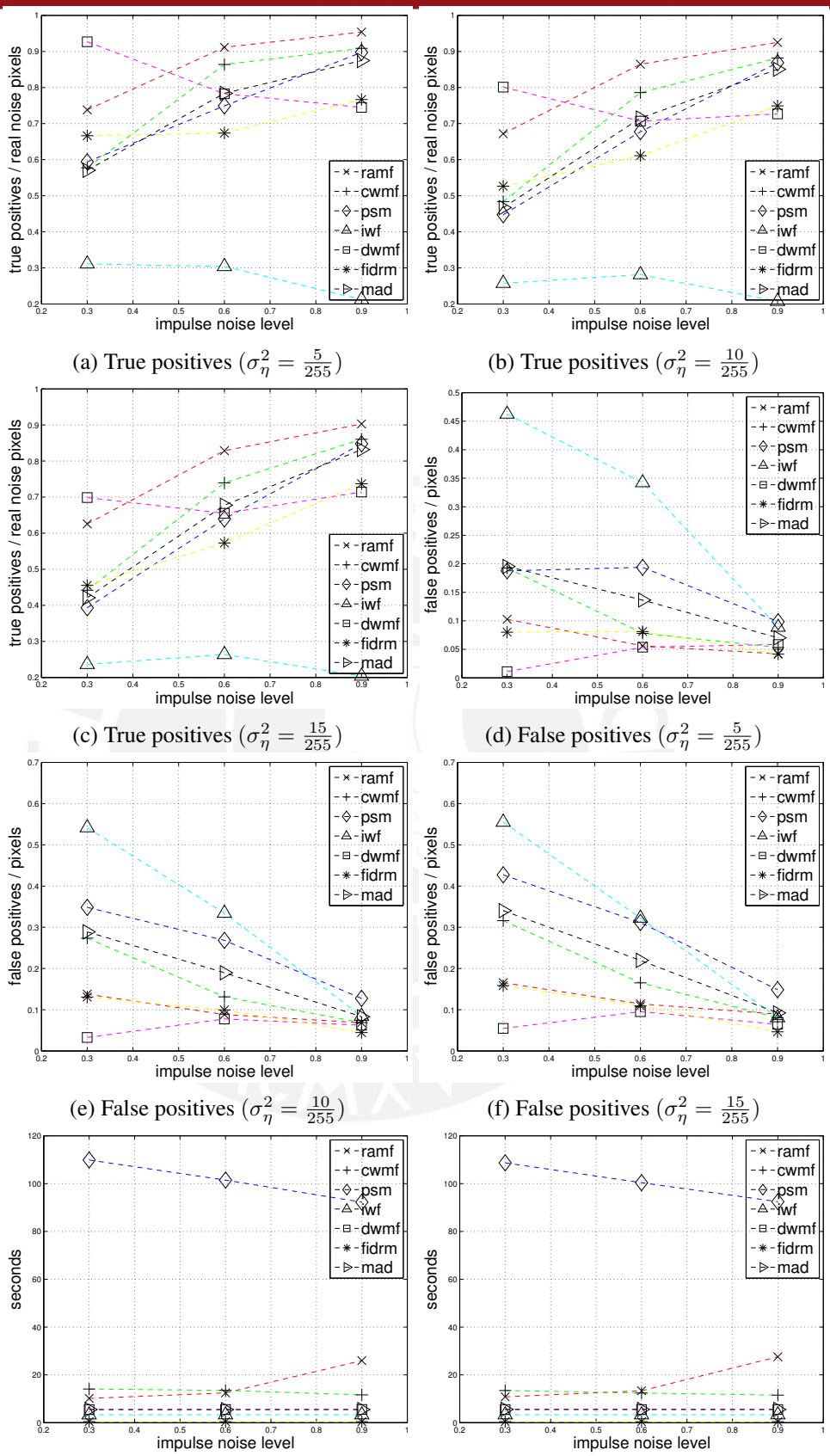

(a) True positives ($\sigma_\eta^2 = \frac{5}{255}$)

(b) True positives ($\sigma_\eta^2 = \frac{10}{255}$)

(c) True positives ($\sigma_\eta^2 = \frac{15}{255}$)

(d) False positives ($\sigma_\eta^2 = \frac{5}{255}$)

(e) False positives ($\sigma_\eta^2 = \frac{10}{255}$)

(f) False positives ($\sigma_\eta^2 = \frac{15}{255}$)

(g) Processing time ($\sigma_\eta^2 = \frac{5}{255}$)

(h) Processing time ($\sigma_\eta^2 = \frac{15}{255}$)

Figure 4.19: Impulse noise detection performance for the Impulse over Gaussian Additive noise scenario for (color layer 1) Goldhill.

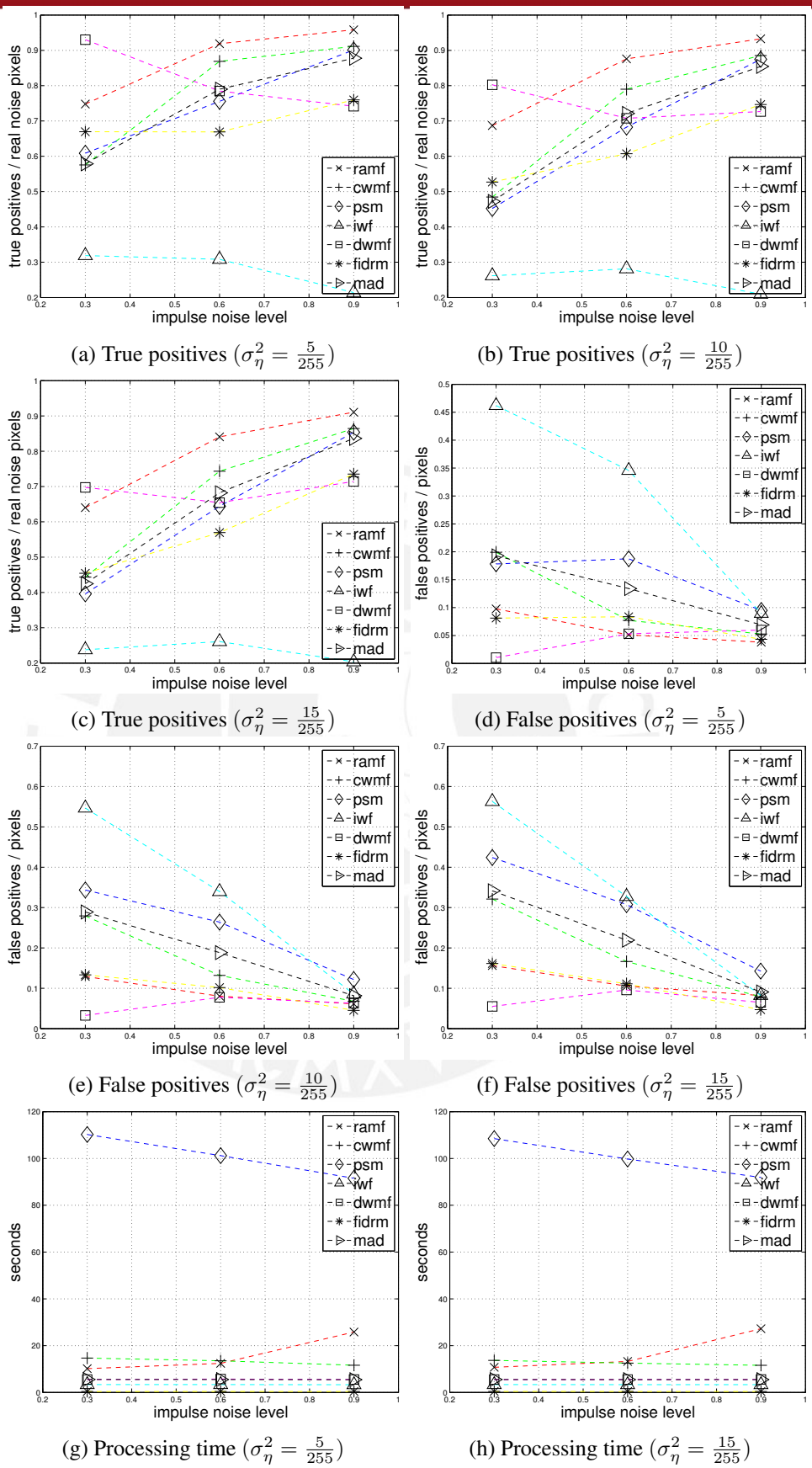

(a) True positives ($\sigma_\eta^2 = \frac{5}{255}$)

(b) True positives ($\sigma_\eta^2 = \frac{10}{255}$)

(c) True positives ($\sigma_\eta^2 = \frac{15}{255}$)

(d) False positives ($\sigma_\eta^2 = \frac{5}{255}$)

(e) False positives ($\sigma_\eta^2 = \frac{10}{255}$)

(f) False positives ($\sigma_\eta^2 = \frac{15}{255}$)

(g) Processing time ($\sigma_\eta^2 = \frac{5}{255}$)

(h) Processing time ($\sigma_\eta^2 = \frac{15}{255}$)

Figure 4.20: Impulse noise detection performance for the Impulse over Gaussian Additive noise scenario for (color layer 2) Goldhill.

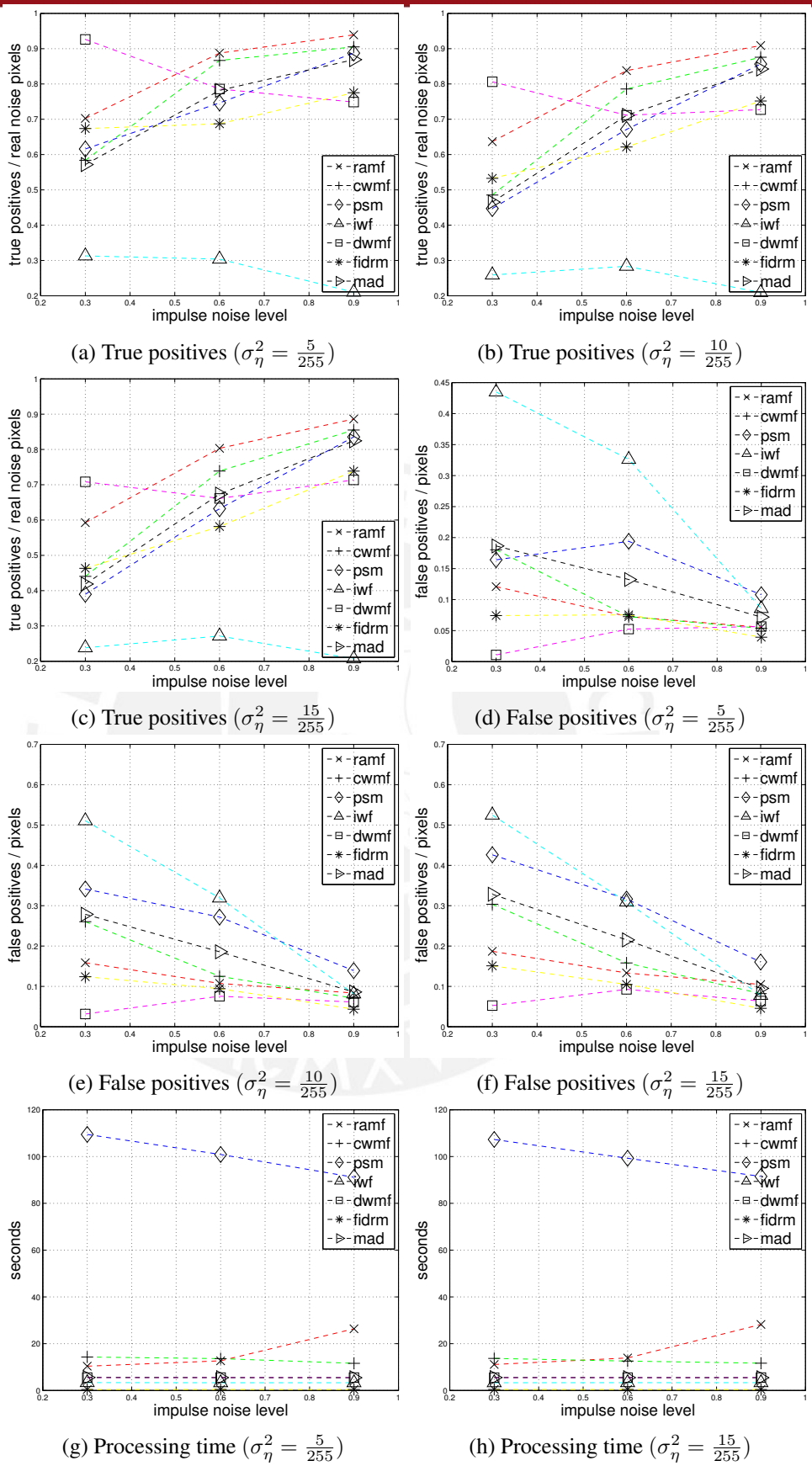

(a) True positives ($\sigma_\eta^2 = \frac{5}{255}$)

(b) True positives ($\sigma_\eta^2 = \frac{10}{255}$)

(c) True positives ($\sigma_\eta^2 = \frac{15}{255}$)

(d) False positives ($\sigma_\eta^2 = \frac{5}{255}$)

(e) False positives ($\sigma_\eta^2 = \frac{10}{255}$)

(f) False positives ($\sigma_\eta^2 = \frac{15}{255}$)

(g) Processing time ($\sigma_\eta^2 = \frac{5}{255}$)

(h) Processing time ($\sigma_\eta^2 = \frac{15}{255}$)

Figure 4.21: Impulse noise detection performance for the Impulse over Gaussian Additive noise scenario for (color layer 3) Goldhill.

(a) $(\sigma_\eta^2, s) = (\frac{5}{255}, 0.3)$ noise corrupted image.

(b) $(\sigma_\eta^2, s) = (\frac{5}{255}, 0.3)$ restored image (PSNR: 34.23 dB).

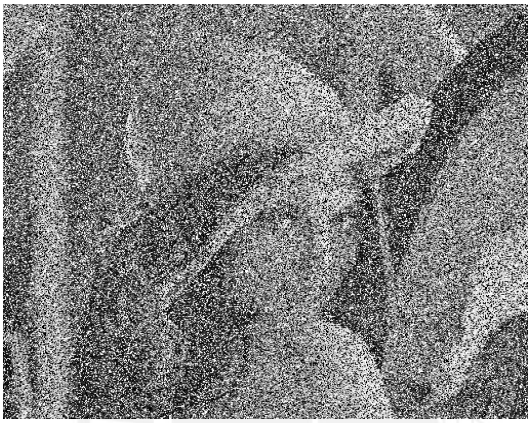

(c) $(\sigma_\eta^2, s) = (\frac{10}{255}, 0.5)$ noise corrupted image.

(d) $(\sigma_\eta^2, s) = (\frac{10}{255}, 0.5)$ noise restored image (PSNR: 31.99 dB).

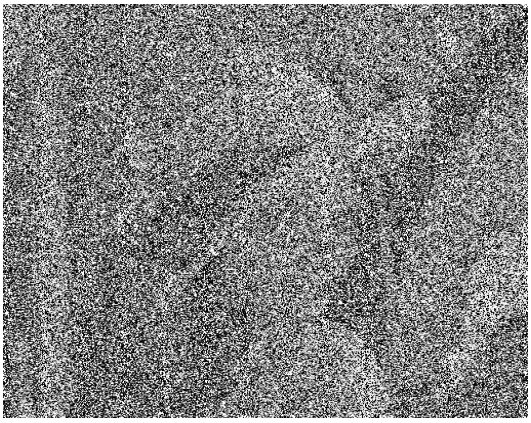

(e) $(\sigma_\eta^2, s) = (\frac{15}{255}, 0.7)$ noise corrupted image.

(f) $(\sigma_\eta^2, s) = (\frac{15}{255}, 0.7)$ noise restored image (PSNR: 29.74 dB).

Figure 4.22: Impulse over Gaussian Additive Noise image denoising for (gray) Lena.

(a) $(\sigma_\eta^2, s) = (\frac{5}{255}, 0.3)$ noise corrupted image.

(b) $(\sigma_\eta^2, s) = (\frac{5}{255}, 0.3)$ restored image (PSNR: 31.01 dB).

(c) $(\sigma_\eta^2, s) = (\frac{10}{255}, 0.5)$ noise corrupted image.

(d) $(\sigma_\eta^2, s) = (\frac{10}{255}, 0.5)$ noise restored image (PSNR: 29.01 dB).

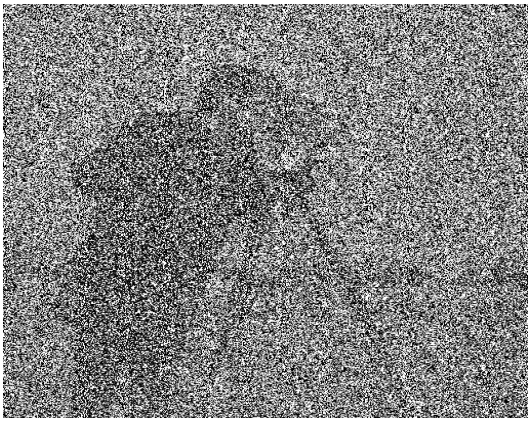

(e) $(\sigma_\eta^2, s) = (\frac{15}{255}, 0.7)$ noise corrupted image.

(f) $(\sigma_\eta^2, s) = (\frac{15}{255}, 0.7)$ noise restored image (PSNR: 27.40 dB).

Figure 4.23: Impulse over Gaussian Additive Noise image denoising for (gray) Cameraman.

(a) $(\sigma_\eta^2, s) = (\frac{5}{255}, 0.3)$ noise corrupted image.

(b) $(\sigma_\eta^2, s) = (\frac{5}{255}, 0.3)$ restored image (PSNR: 30.15 dB).

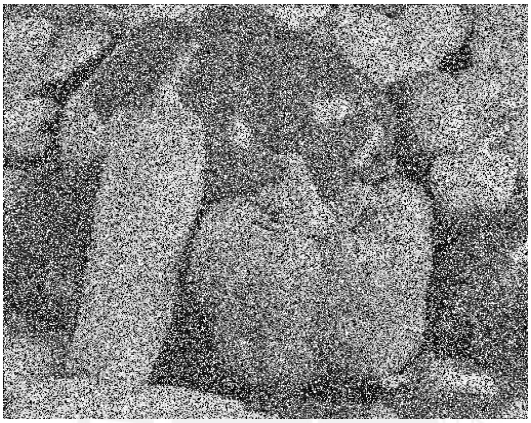

(c) $(\sigma_\eta^2, s) = (\frac{10}{255}, 0.5)$ noise corrupted image.

(d) $(\sigma_\eta^2, s) = (\frac{10}{255}, 0.5)$ noise restored image (PSNR: 28.82 dB).

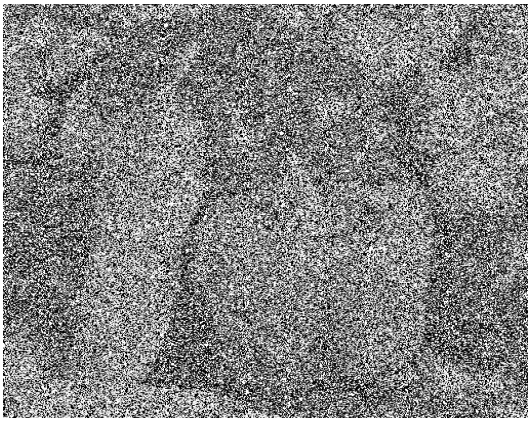

(e) $(\sigma_\eta^2, s) = (\frac{15}{255}, 0.7)$ noise corrupted image.

(f) $(\sigma_\eta^2, s) = (\frac{15}{255}, 0.7)$ noise restored image (PSNR: 27.30 dB).

Figure 4.24: Impulse over Gaussian Additive Noise image denoising for (gray) Peppers.

Chapter 5

Conclusions

The present work proposes a novel automatic Total Variation optimal regularization parameter selection method for image restoration under two different noise scenarios: Impulse and Impulse over Gaussian Additive noise. As main feature, the approach extends the Total Variation formulation to a more suitable cost function, which deals more efficiently with the noise scenarios of interest by penalizing each pixel in a custom way. Thus, the proposed method introduces the following properties:

- It automatically estimates the noise pixel set for both noise models. Furthermore, it estimates the Impulse noise level and the local variance for Gaussian Additive noise.
- It applies an elementwise regularization criteria for each noise model. Based on the estimated noise properties and the noise set estimation, the proposed scheme allows to define a particular regularization level for each noisy pixel in the image, discriminating between noise models while leaving the non-corrupted ones unaltered.
- It updates each regularization parameter by using an iterative scheme. An accurate approach for automatically selecting each regularization parameter by a local-based risk estimator for the Gaussian Additive corrupted pixels, and a novel penalization method based on previous preliminary works for the Impulse noise pixels is applied to define the penalization level in a spatially adaptive form.

The resulting algorithm is proven to be comparable with the state of the art reconstruction quality, although it also shows a dramatical limitation due to its required processing time. Even when there is no considerable improvement in most quality metrics, results show that a more accurate structure response is obtained in contrast to the state of the art algorithms. Future research topics may include the following in order to attack the main drawbacks: (i) the use of a more complex noise estimation algorithm that enhances the actual true positives - false positives ratio; (ii) a less expensive risk estimation method which considerably reduces the actual computational cost; and (iii) a novel Total Variation cost function which includes the Gaussian Additive over Impulse noise scenario, allowing a genuine general Mixed noise scenario.

Bibliography

[1] R. Rojas and P. Rodríguez, "Spatially Adaptive Total Variation Image Denoising Under Salt And Pepper Noise," in *European Signal Processing Conference*, 2011, pp. 278–282.

[2] R. H. Chan, C. Ho, and M. Nikolova, "Salt-and-Pepper noise removal by Median-Type noise detectors and detail preserving regularization," *IEEE Transactions on Image Processing*, vol. 14, no. 10, pp. 1479–1485, 2005.

[3] Y. Xiao, T. Zeng, J. Yu, and M. K. Ng, "Restoration of images corrupted by mixed Gaussian-Impulse noise via $l_1 - l_0$ minimization," *Pattern Recognition*, vol. 44, no. 8, pp. 1708–1720, 2011.

[4] P. Rodríguez, R. Rojas, and B. Wohlberg, "Mixed Gaussian-Impulse Noise Image Restoration via Total Variation," in *IEEE International Conference on Acoustics, Speech, and Signal Processing*, Kyoto, Japan, Mar. 2012.

[5] C. Vogel, *Computational Methods for Inverse Problems*, Society for Industrial and Applied Mathematics, 2002.

[6] T. Chan and J. Shen, *Image Processing and Analysis: Variational, Pde, Wavelet, and Stochastic Methods*, Society for Industrial and Applied Mathematics, 2005.

[7] L. Vese and S. Osher, "Modeling Textures with Total Variation Minimization and Oscillating Patterns in Image Processing," *Journal of Scientific Computing*, vol. 19, no. 1-3, pp. 553–572, 2003.

[8] S. Ramani, T. Blu, and M. Unser, "Monte-Carlo SURE: A black-box optimization of regularization parameters for general denoising algorithms," *IEEE Transactions on Image Processing*, vol. 17, no. 9, pp. 1540–1554, 2008.

[9] Y. Lin, B. Wohlberg, and H. Guo, "UPRE method for Total Variation parameter selection," *IEEE Signal Processing*, vol. 90, no. 8, pp. 2546–2551, 2010.

[10] T. Chan, S. Esedoglu, F. Park, and A. Yip, "Recent developments in Total Variation image restoration," in *In Mathematical Models of Computer Vision*, 2005.

[11] T. Goldstein and S. Osher, "The Split Bregman method for L1-regularized problems," *SIAM Journal on Imaging Sciences*, vol. 2, pp. 323–343, 2009.

[12] Y. Dong, M. Hintermüller, and M. Rincon-Camacho, "A Multi-Scale Vectorial ℓ^p-TV Framework for Color Image Restoration," *International Journal of Computer Vision*, vol. 92, no. 3, pp. 296–307, 2011.

[13] T. Lin, "Adaptive median type filter based on Dempster-Shafer evidence theory for fuzzy image restoration," in *IEEE International Conference on Fuzzy Systems*, 2007, pp. 1–6.

[14] M. Nikolova, "A variational approach to remove outliers and Impulse noise," *Journal of Mathematical Imaging and Vision*, vol. 20, pp. 99–120, 2004.

[15] S. Morillas, V. Gregori, and A. Hervás, "Fuzzy peer groups for reducing mixed Gaussian-Impulse noise from color images," *IEEE Transactions on Image Processing*, vol. 18, no. 7, pp. 1452–1466, 2009.

[16] E. Abreu, M. Lightstone, S. K. Mitra, and K. Arakawa, "A new efficient approach for the removal of Impulse noise from highly corrupted images," *IEEE Transactions on Image Processing*, vol. 5, no. 6, pp. 1012–1025, 1996.

[17] L. Rudin, S. Osher, and E. Fatemi, "Nonlinear Total Variation based noise removal algorithms," *Physica D*, vol. 60, pp. 259–268, 1992.

[18] M. Zhu, S. Wright, and T. Chan, "Duality-based algorithms for total-variation-regularized image restoration," *Computational Optimization and Applications*, vol. 47, no. 3, pp. 377–400, 2010.

[19] T. Chan and S. Esedoglu, "Aspects of Total Variation Regularized L^1 Function Approximation," *SIAM Journal on Applied Mathematics*, vol. 65, no. 5, pp. 1817–1837, 2005.

[20] D. M. Strong and T. F. Chan, *Relation of regularization parameter and scale in Total Variation based image denoising*, CAM Report 96-7. Deptartment of Mathematics, University of California, Los Angeles, 1996.

[21] P. Rodríguez and B. Wohlberg, "Efficient minimization method for a generalized Total Variation functional," *IEEE Transactions on Image Processing*, vol. 18, no. 2, pp. 322–332, 2009.

[22] M. Nikolova, "Minimizers of Cost-Functions Involving Nonsmooth Data-Fidelity Terms. Application to the Processing of Outliers," *SIAM J. Numerical Analysis*, vol. 40, no. 3, pp. 965–994, 2002.

[23] X. Zhu and P. Milanfar, "Automatic parameter selection for denoising algorithms using a No-Reference measure of image content," *IEEE Transactions on Image Processing*, vol. 19, no. 12, pp. 3116–3132, 2010.

[24] H. Hwang and R. Haddad, "Adaptive median filters: new algorithms and results," *IEEE Transactions on Image Processing*, vol. 4, no. 4, pp. 499–502, 1995.

[25] Z. Wang and D. Zhang, "Progressive switching median filter for the removal of Impulse noise from highly corrupted images ," *IEEE Transactions on Circuits and Systems II: Analog and Digital Signal Processing*, vol. 46, no. 1, pp. 78–80, 1999.

[26] R. Garnett, T. Huegerich, C. Chui, and W. He, "A universal noise removal algorithm with an Impulse detector," *IEEE Transactions on Image Processing*, vol. 14, no. 11, pp. 1747–1754, 2005.

[27] C. Tomasi and R. Manduchi, "Bilateral Filtering for Gray and Color Images," in *Proceedings of the Sixth International Conference on Computer Vision*, 1998, pp. 839–846.

[28] Y. Dong and S. Xu, "A new directional weighted median filter for removal of random-valued Impulse noise," *IEEE Signal Processing Letters*, vol. 14, no. 3, pp. 193–196, 2007.

[29] S. Schulte, M. Nachtegael, V. De Witte, D. Van der Weken, and E. Kerre, "A fuzzy Impulse noise detection and reduction method," *IEEE Transactions on Image Processing*, vol. 15, pp. 1153–1162, 2006.

[30] D. Van De Ville, M. Nachtegael, D. Van der Weken, E. Kerre, W. Philips, and I. Lemahieu, "Noise reduction by fuzzy image filtering," *IEEE Transactions on Fuzzy Systems*, vol. 11, no. 4, pp. 429–436, 2003.

[31] S. Aja-Fernández, G. Vegas-Sánchez-Ferrero, M. Martín-Fernández, and C. Alberola-López, "Automatic noise estimation in images using local statistics. Additive and multiplicative cases," *Image and Vision Computing*, vol. 27, no. 6, pp. 756–770, 2009.

[32] P. Rodríguez and B. Wohlberg, "A generalized vector-valued Total Variation algorithm," in *Proceedings of the International Conference on Image Processing*, 2009, pp. 1309–1312.

[33] R. Wolke and H. Schwetlick, "Iteratively Reweighted Least Squares: Algorithms, Convergence Analysis, and Numerical Comparisons," *SIAM Journal on Scientific and Statistical Computing*, vol. 9, no. 5, pp. 907–921, 1988.

[34] Y. Dong, M. Hintermüller, and M. Rincon-Camacho, "Automated regularization parameter selection in multi-scale Total Variation models for image restoration," *Journal of Mathematical Imaging and Vision*, vol. 40, no. 1, pp. 82–104, 2011.

[35] J. Cai, R. H. Chan, and M. Nikolova, "Fast Two-Phase image deblurring under Impulse noise," *Journal of Mathematical Imaging and Vision*, vol. 36, no. 1, pp. 46–53, 2010.

[36] Z. Wang, A. Bovik, H. Sheikh, and E. Simoncelli, "Perceptual image quality assessment: from error visibility to structural similarity," *IEEE Transactions on Image Processing*, vol. 13, no. 4, pp. 600–612, 2004.